García Martínez, A.; Carlucci, P.; Monsalve-Serrano, J.; Valletta, A.; Martínez-Boggio, SD. (2021). Energy management optimization for a power-split hybrid in a dual-mode RCCI-CDC engine. Applied Energy. 302:1-21. https://doi.org/10.1016/j.apenergy.2021.117525

Energy management optimization for a Power-Split hybrid in a Dual-Mode RCCI-CDC engine

Antonio García[*, a], Paolo Carlucci[b], Javier Monsalve-Serrano[a], Andrea Valletta[b] and Santiago Martínez-Boggio[a]

[a] CMT - Motores Térmicos, Universitat Politècnica de València, Camino de Vera s/n, 46022 Valencia, Spain
[b] Università del Salento, Piazza Tancredi, 7, 73100 Lecce, Italy

Applied Energy
Volume 302, 15 November 2021, 117525
https://doi.org/10.1016/j.apenergy.2021.117525

Corresponding author (*):
Dr. Antonio García Martinez (angarma8@mot.upv.es)
Phone: +34 963876559
Fax: +34 963876559

Abstract

The electrification of propulsion systems in light passenger vehicles is essential to reach the objectives set by the different organizations that protect the environment. However, due to various aspects such as politician decisions, bad press, high powertrain production costs and a moderate reduction in energy consumption, purely electric vehicles are being a priority for several car manufacturers as well as for governments instead of hybrid vehicles. This article shows how hybrid electrification, using a low temperature combustion engine, is capable of reducing the energy consumption while drastically minimizing the particle matter (mainly soot) and NOx emissions, in a power split propulsion system. This is possible by means of a precise control of the operating conditions of the engine. To operate in the hybrid powertrain efficiently and with low emissions, several energy managements controller strategies are studied. In this work, adaptive Equivalent Minimization Control Strategy (ECMS) and Rule-Based Control (RBC) are used as online controller, and the dynamic programming optimal control is used to size the powertrain. In this sense, the electric machine maximum power, battery energy content, power split device gear ratio as well as the control parameter are studied. Both emissions and fuel consumption are included in the optimization function. The results show that it is possible to reduce the fuel consumption by 17.5% with an energy minimization-oriented strategy. In addition, ECMS is more effective to control both emissions and fuel economy. If a double target is applied, the fuel consumption is reduced to 5% while achieving Euro 6 emissions levels without the need for NOx and particulate matter aftertreatment systems. This strongly reduces the total cost of the propulsion system compared to a conventional vehicle, thus compensating the cost increase due to the hybridization without considering the fuel saving costs.

Keywords

RCCI, Energy Management, ECMS, Hybrid powertrain, Emissions regulations

1. Introduction

Advanced combustion technologies represent a valuable option to meet the new limitations imposed to internal combustion engines in terms of greenhouse gases (GHG) and harmful pollutants emissions [1]. Other option, more used nowadays, is the use of complex aftertreatment systems (ATS). The main reason is the effectiveness to reduce emissions with low system control complexity. However, the global context is shifting towards a stricter era of polluting emissions and electrification. Therefore, the current ATS will not achieve future emissions levels without the engine modification to reduce the raw engine-out emissions. Also, the increase in cost and size of more complex ATS make a favorable scenario for advanced combustion concepts as low temperature combustion (LTC). In spite of LTC being able to reduce NOx and particle matter (PM) among others, it is not possible to strongly reduce the CO_2 emissions. The maximum brake thermal efficiency (BTE) of the LTC modes is close to a conventional diesel combustion (CDC). Therefore, powertrain electrification is crucial for the overall vehicle efficiency improvement [2]. The degree of improvement depends on the value of the hybridization factor but also the type of hybrid architecture [3] and control system [4]. In this sense, also the supervisory control strategies play a fundamental role since the actuation of the electric machine/s and the ICE should be optimally coordinated [5].

Low temperature combustion modes (LTC) for compression ignition engines (CI) have a great potential due to offering ultra-low NOx and soot emissions together with high brake thermal efficiency [6]. Several research centers are developing different LTC strategies as the homogeneous charge compression ignition (HCCI) [7], partially premixed combustion (PPC) [8], premixed charge compression ignition (PCCI) [9], reactivity controlled compression ignition (RCCI) [10] and gasoline compression ignition (GCI) [11]. They are differentiated by the injection strategy and the fuel composition as well as the number of fuels used. For example, the RCCI concept uses two fuels with different reactivity to control the ignition timing and the heat release rate profile promoting early injection timings to ensure a sufficient air–fuel mixing before the combustion to avoid the soot production [12][13]. Unfortunately, none of the proposed LTC modes can cover the entire engine map due to the excessive pressure gradients that appear at high loads and the low combustion efficiency that occurs under low load conditions. Therefore, these combustion concepts are still limited to moderate loads within the engine map. Garcia et al. [14] combines RCCI in low and medium loads with conventional diesel combustion (CDC) at high load in order to allow the operation in all the engine map. In spite of the advantages that this multi-mode combustion approach offers in terms of NOx and soot emissions, in a conventional non-hybrid and parallel hybrid powertrain, it was not possible to achieve the engine-out Euro 6 emissions levels due to transient peaks in CDC combustion [15]. Also, both powertrains not allow a controlled engine operation in the RCCI zone.

Many hybrid electric architectures have been introduced in the market up to now: the series architecture was among the first to be used [16], but nowadays it is hardly employed [17]; the parallel configuration has gained a lot of success especially with the

mild-hybrid vehicles, but it can offer remarkable advantages at low integration efforts with respect to the conventional no-hybrid platforms. The pros and cons of the two solutions are well known, for example the series hybrid requires the implementation of two powerful electric machines, but in this case the ICE can be operated at will being it decoupled from the driven wheels; the parallel hybrid only asks for one electric machine, but the ICE is coupled to the driven wheels and its operation can be improved only through a suitable energy split with the EM. In addition, as in a non-hybrid powertrain, the ICE suffers hard transient conditions due to the vehicle speed dependency. A third commonly diffused architecture exists, the so-called power-split, which was introduced by Toyota with the name "Toyota Hybrid System" (THS) [18,19]. The peculiarity of this solution is the planetary transmissions through which the ICE can simultaneously be controlled independently from the wheel dynamics and output traction power to satisfy the power demand [20]. Since the first appearance in the market in 1999, the THS has undergone several upgrades, but also other car manufacturers have suggested different uses of the planetary transmission in an automotive powertrain. In addition, other than the powertrain architecture, the control strategy, which is in charge of coordinating the power split between the ICE and EMs, has a very important job that is the key to fuel consumption and emissions production [21]. In the scientific literature [22], the equivalent minimization control strategy has shown good characteristics in terms of design and implementation for HEV powertrain control. However, in the case of the power-split HEV few examples can be found: the work of Zou et al. [23] is an interesting example that presents a similar implementation of the ECMS algorithm as the one used in this work.

The goal of this work is to complement the study on the feasibility and potentials of the implementation of the dual-mode RCCI-CDC engine, operating under the RCCI and CDC technologies in a power split hybrid electric vehicle. The methodology used to assess the potential of this concept is the same used for the P2-parallel HEV in previous work [14]. At first, the optimal components sizing is investigated with DP, then the powertrain is studied in the situation where it is controlled via a real-time energy management control strategy. The WLTC driving cycle, which is used for the vehicle homologation, is adopted to test the vehicle's fuel consumptions and emissions. Therefore, the main novelty of the work is to show the effect of different energy management strategies to precisely control the ICE operation with an advanced combustion mode. This methodology is aimed to achieve both the energy consumption reduction and achieve ultra-low engine-out emissions. The work is based in a power-split full HEV architecture for a passenger car. In addition, this manuscript brings more novelties in terms of proposing a sizing methodology based in an optimal algorithm as the Dynamic Programming. To apply in a real-demonstrator, a rule based and energy consumption minimization strategy on-line algorithms are calibrated. The paper content is structured to introduce the reader to: the dual-mode RCCI-CDC engine, HEV power-split powertrain characteristics; the sizing methodology based on DP; the design of the on-line control strategies and, finally, the results. To increase the manuscript overview,

results from a previous parallel hybrid study under the same conditions are added in the conclusions section.

2. Materials and Methods

2.1. Dual-Mode RCCI-CDC

The RCCI technology was investigated in a single-cylinder engine that had the characteristics of a commercial GM 1.9L four-cylinder turbo diesel engine. The commercial ICE was calibrated by the OEM to homologate under Euro 4 legislation. RCCI combustion requires the in-cylinder mixing of two fuels that have different reactivity: the data used in this work are derived from experimental data where the low reactivity fuel is gasoline and the high reactivity fuel is diesel. Hence the engine retrofit just involved to integrate a secondary fuel injection at cylinder intake port (PFI). Table 1 summarizes the most relevant characteristics of the engine. More details of the test bed configuration and characteristics can be found in previous works [24,25].

Table 1. Single cylinder engine characteristics adapted from a 1.9 GM CI Engine.

Engine Type	4 stroke, 4 valves, direct injection
Number of cylinders	1
Displaced volume	477 cm^3
Stroke	90.4 mm
Bore	82 mm
Piston bowl geometry	Re-entrant
Compression ratio	17.1:1
Rated power @ 4000 rpm	27.5 kW
Rated torque@ 2000-2750 rpm	80 Nm

The operation of the RCCI combustion is limited to the medium loads, since at higher IMEP the high stock compression ratio of the engine caused too early autoignition of the mixture, which led to excessive pressure rise rates. At high engine speeds, it is not possible to work with a single-cylinder engine due to mechanical limitations of the testbed. For this reason, conventional diesel combustion (CDC) is actuated beyond the limits of RCCI to enable a reliable usage of the full engine map: the concept is named dual-mode RCCI-CDC . The most significant maps are reported from Figure 1: the black points indicate the successful calibration of the RCCI combustion mode, while the white points are operated with CDC. Overall, the main advantage of RCCI combustion is the low temperature characteristic, which improves the break thermal efficiency of the engine due to the lower heat losses [26], and thanks to the premixed nature of the charge together with the high EGR rates (average of 40%) it enables to achieve ultra-low NOx and soot engine-out emissions simultaneously. However, at the low loads, due to

the low temperatures, the increase of HC and CO emissions requires serious consideration for the implementation of a reliable DOC converter in the aftertreatment system. In this sense, conventional converters are not enough unless the catalyst size is increased [27], so that novel technologies should be explored, such as the use of novel catalytic additives proposed in the work conducted by Binder et al. [28,29]. Further information about RCCI testing and the dual-mode RCCI-CDC concept can be collected from other works of the authors [30–32].

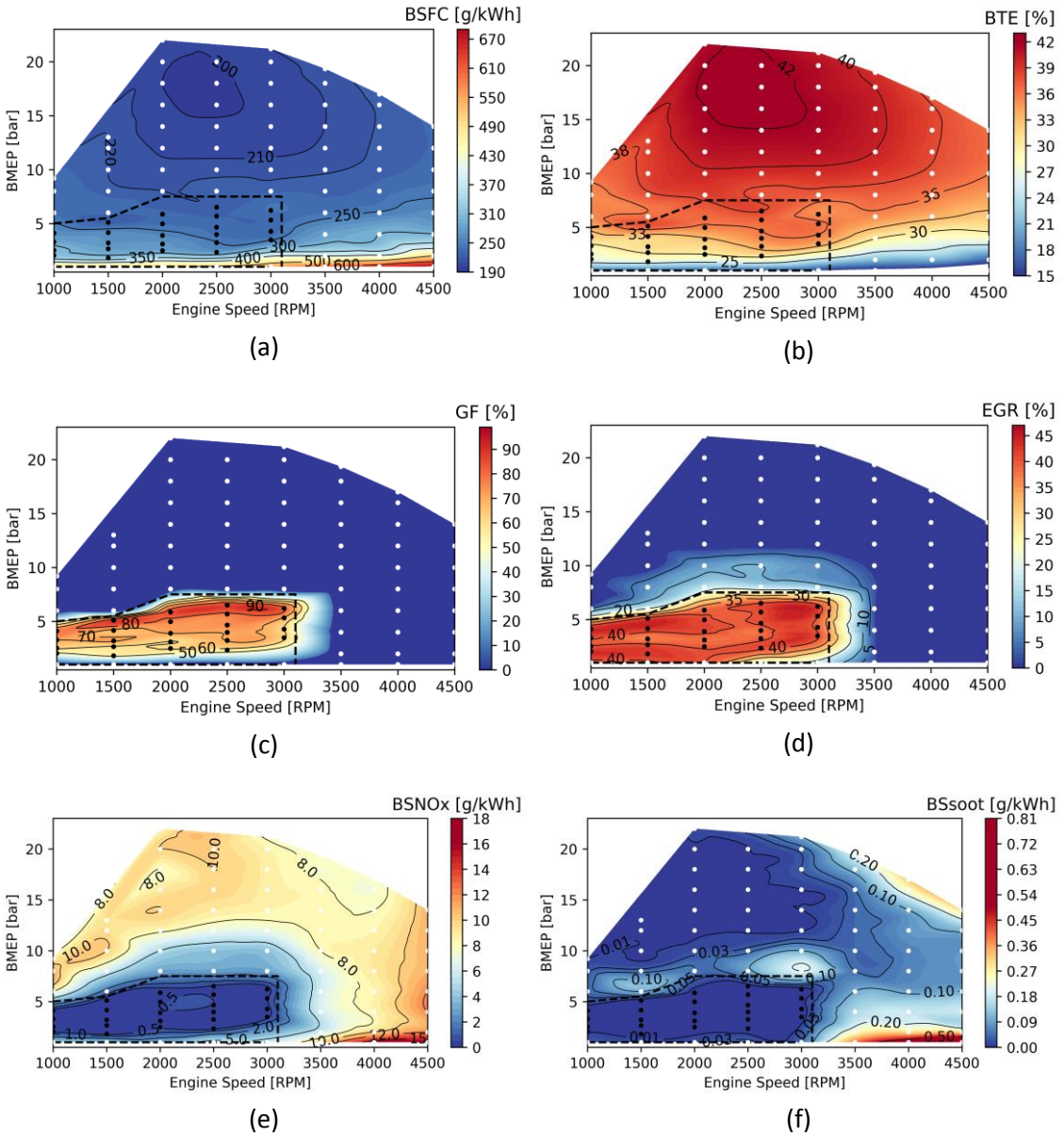

Figure 1 – Brake specific fuel consumption (a), brake thermal efficiency (b), Gasoline fraction (GF) (c), exhaust gas recirculation (EGR) rate (d), Brake specific NOx emissions (e) and brake specific soot emissions (f) for the dual-mode RCCI-CDC calibration concept.

2.2. Full electric hybrid Power-split vehicle model

In the power-split HEV powertrain architecture, the planetary transmission is used as a speed coupling device. Figure 2 shows that the ICE is coupled to the carrier gear, one electric machine (EM1) is connected to the sun and the other one (EM2) to the ring.

Finally, the differential/final-drive is the torque-coupling device and it is linked to the ring gear. The planetary transmission enables to split the engine power between two paths: the electrical path, where part of the power delivered by the ICE is sent to EM1 (generator mode) and stored in the battery or directly sent to the motor EM2 (traction mode) via a controlled power bus, and the mechanical path that brings the remaining power to the transmission output.

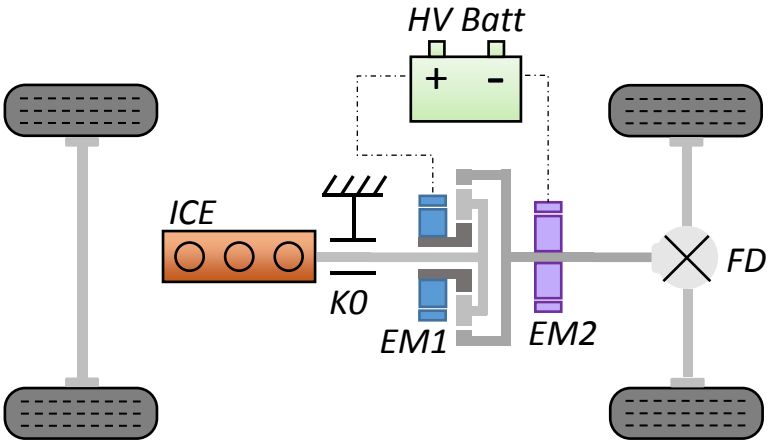

Figure 2 – Power-split e-CVT hybrid vehicle. ICE-internal combustion engine, EM1-motor/generator 1, EM2-motor/generator 2, K0-clutch, FD-final drive, HV Batt-high voltage battery

The clutch K0 differentiates this architecture from the original one adopted by Toyota for the first generation of the Prius. The clutch introduces another operating mode, in fact the carrier ring of the planetary transmission, hence the ICE, can be grounded so that the vehicle can operate in pure electric driving mode. Considering the torque demand at the wheels, the torque at the final-drive input $T_{FD,in}$ can be calculated with the final-drive ratio τ_{FD} and its efficiency ${\eta_{FD}}^{v}$ (the exponent $v = 1$ when $T_{wheels} > 0$ and $v = -1$ when $T_{wheels} < 0$):

$$T_{FD,in} = \frac{T_{wheels}}{\tau_{FD}{\eta_{FD}}^{v}} \tag{1}$$

Also, the input shaft speed ($\omega_{FD,in}$), which is connected to the ring gear (ω_r) of the planetary transmission, is calculated from the vehicle speed $v_{vehicle}$ and the wheel radius (R_{wheel}):

$$\omega_{FD,in} = \omega_r = \frac{v_{vehicle}}{R_{wheel}}\tau_{FD} \tag{2}$$

Solving the forces balance in the power split device and the rotational speed dependency between the components (ICE, EM1 and EM2) it is possible to understand the powertrain behavior. A detailed explanation was added in the Appendix A.

$$\begin{cases} P_s = -\dfrac{1}{(K+1)}P_c\dfrac{\omega_s}{\omega_c}{\eta_{ps}}^{q} \\ P_r = P_{load} - \dfrac{K}{(K+1)}P_c\dfrac{\omega_r}{\omega_c}{\eta_{ps}}^{q}{\eta_{pr}}^{t} \end{cases} \tag{3}$$

where the subscripts “s”, “r” and “c” indicate the sun, the ring and the carrier gears respectively. K is the transmission ratio in the power split device ($K = \frac{\omega_s}{\omega_r}$), P_{load} is the power demand and η_{ps}, η_{pr} the efficiency in the power split transmission.

It can be understood that the way in which the ICE power is split into the mechanical and electrical paths depends on two aspects: first, the torque exerted by EM1 is linked to the ICE one through the planetary transmission ratio K; second, the speeds of the ICE and EM1 depend both on the transmission ratio K and on the ring speed. This suggests that there is the possibility to conveniently regulate the ICE operation so that it works at its best efficiency. In order to have an ICE speed greater than idle (i.e 850 rpm), especially at moderate vehicle speeds, EM1 has to rotate in the positive direction (same as the ICE). Therefore, EM1 supplies a negative power and it works as a generator. Part of the ICE power is hence absorbed by EM1 and the remaining part is transferred to the ring gear [33]. On the other hand, if the vehicle speed is too high and the clutch K0 is opened, the angular speed of EM1 may fall to zero or can even turn negative (opposite to the ICE speed): in this particular condition, EM1 absorbs no power (zero EM1 speed) or outputs positive power, hence all the power produced by the ICE is output to the ring gear. In this case, EM2 modulates the power output from the ring gear to satisfy the power demand at the wheels by working in generator mode: this situation is called “re-circulation”. This mode of operation is not efficient since the power flow undergoes many mechanical-to-electrical conversions and vice-versa [34].

The EM1 regulates the ICE speed, but at the same time the torque output of EM1 must balance the torque output from the carrier gear. This implies that the desired torque signal to actuate EM1 (T_{EM1}) is made of two parts, as also discussed in [35]: a feed-forward part and a feed-back one. Figure 3 represents the concept of the EM1 feed-forward and feed-back controller used in the modeling of the power-split HEV.

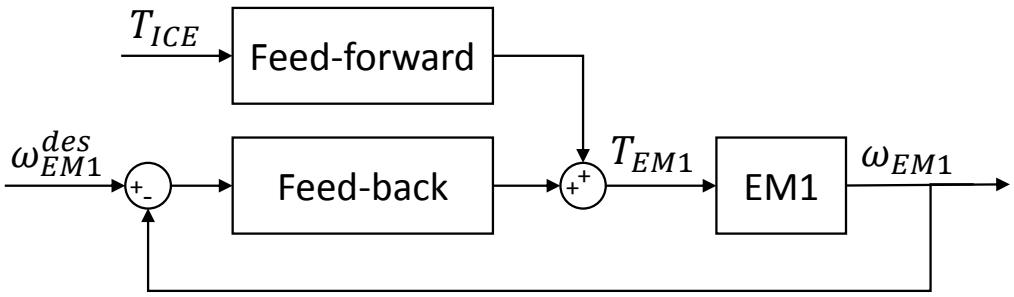

Figure 3 – EM1 feed-forward and feed-back controller for the torque output. Reprint from [35].

The last part is needed to track the reference speed signal. The resulting torque signal for EM1 can therefore be written by considering a PID (K_P, K_I, K_D) type feedback control:

$$T_{EM1} = -\frac{1}{(K+1)} T_{ICE} {\eta_{ps}}^{q} + \\ + \left[K_P(\omega_{EM1}^{des} - \omega_{EM1}) + K_I \int (\omega_{EM1}^{des} - \omega_{EM1}(\tau))\, d\tau + K_D \frac{d(\omega_{EM1}^{des} - \omega_{EM1})}{dt} \right] \quad (4)$$

The PID tuning of the EM1 controller is fundamental for a correct functioning of the system: overshoots must be prevented with anti-windup solutions. In fact, as the EM1 power output is constrained, for example by its mechanical limitations and also by the battery BMS limitations, the EM1 controller can saturate and windup eventually occurs, so it will produce a too high EM1 torque (overshoot) which will accelerate the ICE away from the target optimal speed. An advanced anti-windup function is implemented into the built-in GT-Suite PID block.

There exist other types of architectures which use planetary transmission devices and have this CVT function: they can be classified in input-split, output-split and compound split [36]. The difference lies in the location of the power-split devices.

2.3. Energy management system

2.3.1. Dynamic Programming

The EM coupled to the sun gear of the planetary transmission, must have a rotational speed range that can sustain the regime of operation of the engine for different vehicle speeds, and it must be able to absorb the necessary power which is transferred from the ICE to recharge the battery. On the other hand, EM2 must have a power rating such to compensate the ICE power output that flows to the ring gear of the planetary transmission to satisfy the driver power demand. The transmission ratios of both the planetary gear-train and the final drive are also important design parameters since they influence the speed and torque relations between the electric machines and the engine. Finally, the battery capacity should be enough to store at least all the energy recuperated through regenerative braking, but it must as well guarantee adequate ICE boosting and electric drive. Moreover, the number of parallel cells, apart from determining the overall battery capacity, also set the maximum current output. In general, an optimal design of these key powertrain components depends on the way the vehicle is used and on the energy management strategy which regulates the power flow between the ICE and EMs. The sizing procedure is applied in the two scenarios of fuel-economy and engine-out emissions reduction and the WLTC driving cycle can be adopted as the average use case of the vehicle.

For the power-split HEV, there are many design parameters and this fact clearly increases the computational burden for exploring the factorial number of combinations to find the best set. Therefore, a sizing procedure formulated as an optimization problem and solved with Dynamic Programming (DP), is more indicated for the task. A similar study was done by Vinot [37], where different power-split architectures were analyzed and compared through a DP-based global optimal design method. With this shortcut, the list of design parameters is outlined below together with the chosen range of variation (a unique scale factor was used to dilate the map of the EMs):

- Scale factor for EM1 $f_{scale,EM1} \in [0.7, 1.4]$
- Scale factor for EM2 $f_{scale,EM2} \in [0.5, 1.5]$
- Number of parallel cells connections $N_p \in [3, 4]$
- Planetary gear-train transmission ratio $K \in [1.5, 3.5]$

- Final-drive transmission ratio $\tau_{FD} \in [2, 4]$

The initial sizes for the EM1, EM2 and battery capacity were set equal to 30 kW, 50 kW and 6.9 Ah respectively. The EMs sizes are in line with the data available for the Toyota Hybrid System (THS) [38] the battery capacity value corresponds to the optimal one determined for the P2-parallel case [14], obtained with cylindrical A123 (3.3 V and 2.3 Ah) in 3 parallel (6.9 Ah) and 121 series cells (400 V) connections.

The code of the vehicle model to be used with the DP algorithm is built with:

- two control variables (the ICE speed and torque)
- one state variable (the battery SoC).

Although the number of the control variables could be reduced by forcing the ICE to operate on the minimum BSFC line for instance, the following solution would not be optimal. In fact, as explained by Muta et al. [19], the optimal system efficiency does not always correspond to the ICE optimal efficiency point for a given power demand. Moreover, the objective function of the optimization problem is given by the sum of the fuel consumption and NOx emissions by means of a penalty factor β:

$$J(u(t)) = \int_0^{t_f} [\dot{m}_{fuel}(\tau) + \beta \dot{m}_{NOx}(\tau)] d\tau$$

where $u(t)$ is the vector of control variables. To optimize the fuel economy alone, β is set to zero; on the other hand, to also minimize the engine-out emissions of NOx (soot emission levels are always compliant with the regulations) β is set to values not greater than 1000.

Despite using DP for the optimal powertrain design, it is necessary to investigate how online energy management control strategies impact on the final fuel consumption and emissions. In this work, rule-based control (RBC) and adaptive equivalent consumption minimization strategy (a-ECMS) are calibrated and compared against the optimal solution (DP) and the baseline case (non-hybrid diesel powertrain).

2.3.2. Online Management Strategy

On the contrary to DP, online management control strategies do not solve an optimization problem defined all over the time horizon, which is of course unknown a-priori. Furthermore, the additional degree of freedom for powertrain operation, provided by the adoption of the planetary transmission, makes the design and calibration of an RBC strategy trickier. In the original Toyota Hybrid System (THS), a divide-and-conquer architecture is suggested to decouple the multi-input control structure in two parts: the system optimization, which specifies the ICE power demand; the ICE optimization that selects a pre-calculated optimal ICE speed according to the power demand [18,39]. Recalling Figure 3, EM1 is used to achieve the desired ICE speed, however this type of control may be limited by the characteristics of EM1 in terms of torque capability and speed range as it occurred in the first generation of the THS. Moreover, there is always a transient before the target ICE speed is achieved. This issue

was improved with the second generation of the THS by implementing a different generator EM1 (speed range from 6500 rpm to 10000 rpm). EM2 finally complements the power output to satisfy the driver's demand. The same control approach is maintained for the second-generation Prius whose architecture is used in this work.

In the THS, the ICE control may be done by taking into account the minimum BSFC operating line [38], however as also noted in the design phase with DP, the ICE optimal operating region does not necessarily provide the optimal vehicle fuel economy so that it becomes clear that with RBC strategy the task of achieving a good fuel economy is harder than with an adequately designed optimization based control (OBC). As also analyzed in the work of Vinot et al. [34], the target space of operating points of the ICE for the THS concept is represented by a curve, which is obtained during experimental campaigns of the average vehicle use: although it is close to the minimum BSFC line, it does not correspond to it and this suggests once again that the tank-to-wheel efficiency rather than the ICE efficiency alone would determine the best operation of the ICE for the power-split hybrid concept.

2.3.2.1. Rule-Based Control strategy

The RBC control strategy implemented for the power-split HEV is a combination of the thermostat and power follower RBC types. In fact, the power output of the ICE and EM is decided mainly on the traction power demand and the battery SoC level is the most important parameter which decides the switching between the operating modes. Similar to the case of the P2-parallel HEV [14], the RBC control is structured with a state machine: the main operating modes are given as states and the transitions between them are governed by precise rules.

The following Table 2 and Table 3 give information regarding the actuation of the ICE, EM1 and EM2 for each state and the transition rules. The signal of the desired power P_{des} is calculated by the driver PID control. The type of control strategy, as can be inferred from Table 2, is engine-centric, which means that when running under the "HEV drive" mode the entire driver power demand is addressed to the ICE and EM2 has the task to complement it, since not all the power produced by the ICE is actually output at the ring gear. However, during a braking event the ICE can only produce enough power to win the mechanical friction losses and to recharge the battery ($P_{charge} + P_{losses}$): P_{des} is set equal to the regenerative braking power as calculated by the regenerative braking system (RBS) controller. The ICE power should always be lower than its rated maximum power output P_{ICE}^{max}. Also, it should be greater than a minimum value P_{ICE}^{min} which is to be calibrated so to avoid inefficient use of the engine. At any instant, also the mechanical constraints of the two electric machines are satisfied.

The sub-states "boost" and circulation" are reported to indicate that under "HEV drive" mode, according to the speed of EM1 and the power output of the ICE, it may happen that EM2 outputs positive power to aid the ICE (boost), or it may exert a negative power to absorb the extra ICE power output with respect to the one required at the wheels (circulation). Moreover, as already discussed, the EV drive mode can be

performed by EM2 alone, or by EM2 and EM1 simultaneously, since when the ICE is grounded, the planet gears behave as idler gears. However, the rated power of EM2 is enough to cope with the usual demand over a WLTC driving cycle.

It can be noted that there is no state which enables battery recharging when the vehicle is stopped: in this way, the battery SoC level can be sustained only through an adequate control when the vehicle is moving. The vehicle starts moving under EV mode, unless the battery SoC is below a given threshold SoC_{min}: its value can be calibrated and it may be higher than the lower boundary of the admissible SoC range (0.4-0.8). When the ICE is to be switched on, "ICE start" state is enabled and the clutch that grounds the engine is opened. The power request to recharge the battery P_{charge} is produced by a PID controller whose proportional and integral factor must be tuned (K_I^{SoC}, K_P^{SoC}).

Table 2. RBC strategy for the power-split HEV: main states of operation. $\boldsymbol{T_{des}}$ – desired driver torque demand, $\boldsymbol{P_{des}}$ – desired driver power demand, $\boldsymbol{P_{losses}}$ – estimated mechanical power losses of the transmission, $\boldsymbol{P_{ring}}$ – ring output power, $\boldsymbol{P_{ICE}^{idle}}$ – ICE power output at idle, $\boldsymbol{P_{charge}}$ – battery charging power request, $\boldsymbol{P_{ICE}^{min}}$ – minimum ICE power, $\boldsymbol{P_{ICE}^{max}}$ – maximum ICE power.

State	EM1 torque	EM2 power	ICE power
Vehicle Stop	0	0	0
EV drive	$\max_{T_{des}>0}[(T_{des} - T_{EM2}), 0]$	$P_{des} - P_{ring} + P_{losses}$	0
	$\min_{T_{des}<0}[(T_{des} - T_{EM2}), 0]$		
ICE start	T_{EM1}	$P_{des} - P_{ring} + P_{losses}$	P_{ICE}^{idle}
HEV drive	T_{EM1}	$P_{des} - P_{ring}$	$\min[\max[(P_{des} > 0) + P_{charge} + P_{losses}, P_{ICE}^{min}], P_{ICE}^{max}]$

Table 3. RBC strategy for the power-split HEV. Rules for the transitions between the states. $\boldsymbol{v_{veh,des}}$ – desired vehicle speed, $\boldsymbol{v_{EM2,max}}$ – maximum vehicle speed to enable EV drive, $\boldsymbol{SoC_{min}}$ – minimum battery SoC, $\boldsymbol{SoC_{charge,max}}$ – maximum battery SoC, $\Delta\boldsymbol{t}$ – time spent in a state, $\Delta\boldsymbol{t_{min}^{ICE}}$ – minimum time for engine continuous operation.

		States transitions rules
1	Vehicle Stop – EV drive	$v_{veh,des} > 0$ AND $SoC > SoC_{min}$
2	Vehicle Stop – ICE start	$v_{veh,des} > 0$ AND $SoC \leq SoC_{min}$

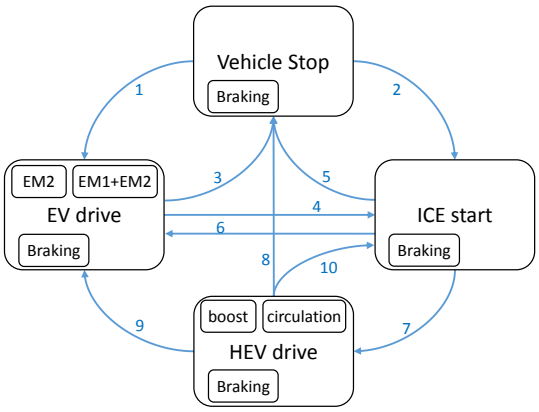

3	EV drive – Vehicle Stop	$v_{veh,des} = 0$
4	EV drive – ICE start	$v_{veh,des} > 0$ AND ($v_{veh} \geq v_{EM2,max}$ OR $SoC \leq SoC_{min}$ OR $P_{des} > P_{EM2,max}$)
5	ICE start – Vehicle Stop	$v_{veh,des} = 0$
6	ICE start – EV drive	$\Delta t > 5$ AND $\omega_{ICE}^{act} < \omega_{ICE}^{idle}$ AND $v_{veh,des} > 0$
7	ICE start – HEV drive	$\omega_{ICE}^{act} > \omega_{ICE}^{idle}$ AND $v_{veh,des} > 0$
8	HEV drive – Vehicle Stop	$v_{veh,des} = 0$
9	HEV drive – EV drive	$\Delta t > \Delta t_{min}^{ICE}$ AND $SoC \geq SoC_{charge,max}$ AND $v_{veh} < v_{EM2,max}$ AND $P_{des} < P_{EM2,max}$ AND $v_{veh,des} > 0$
10	HEV drive – ICE start	$v_{veh,des} > 0$ AND $SoC \leq SoC_{min}$

2.3.2.2. Adaptive Equivalent Consumption Minimization Strategy

The concept behind ECMS is the minimization of the equivalent fuel consumption, which was originally developed for the parallel HEV concept [40], but it can also be applied for the power-split HEV. The equivalent fuel consumption considers the mass of fuel that is actually consumed by the ICE to produce power and an equivalent fuel mass that involves the power produced by EMs. In fact, since HEVs cannot be recharged externally as PHEVs, the battery energy is in the end provided by the ICE and through regenerative braking. The equivalent fuel consumption is thus expressed as follows:

$$\dot{m}_{fuel\ eqv} = \dot{m}_{fuel\ ICE} + \dot{m}_{Batt} = \dot{m}_{fuel} + s_{eqv}\frac{P_{Batt}}{Q_{LHV}} \tag{5}$$

$\dot{m}_{fuel\ ICE}$ is the fuel burnt by the ICE to move the vehicle and it is proportional to the ICE power output P_{ICE}; $\dot{m}_{Batt}$ is the equivalent fuel mass used to sustain the battery SoC level that can be formulated by considering the battery power output P_{Batt} that is multiplied by the low heating value of the fuel Q_{LHV} and at last it is scaled by the equivalence factor s_{eqv}, which must be calibrated. To explicitly consider the efficiency of the ICE, P_{ICE} must be calculated with the fuel mass-flow rate and the low heating value:

$$P_{ICE} = Q_{LHV}\dot{m}_{fuel\ ICE} \tag{6}$$

On the other hand, P_{Batt} is related to the power output of the two electric machines EM1 and EM2:

$$P_{Batt} = P_{EM1}(\eta_{EM1}\eta_{batt})^x + P_{EM2}(\eta_{EM2}\eta_{batt})^y \tag{7}$$

The exponents x and y are equal to -1 when the EM discharges the battery, otherwise they equal to 1. At this point, equation (5) can be written in its full form in terms of powers:

$$P_{fuel\,eqv} = Q_{LHV}\dot{m}_{fuel\,ICE} + s_{eqv}(P_{EM1}(\eta_{EM1}\eta_{batt})^x + P_{EM2}(\eta_{EM2}\eta_{batt})^y) \tag{8}$$

In the power-split HEV powertrain, $P_{EM2} = P_{des} - P_{ring}$ (P_{des} is the driver power demand reduced at the final-drive input). Equation (8) therefore becomes:

$$P_{fuel\,eqv} = Q_{LHV}\dot{m}_{fuel\,ICE} + s_{eqv}\big(P_{EM1}(\eta_{EM1}\eta_{batt})^x + \big(P_{des} - P_{ring}\big)(\eta_{EM2}\eta_{batt})^y\big) \tag{9}$$

The previous formula must be further handled: the objective is to explicitly write the instantaneous cost function of the ECMS problem as a function of the main control variables. It is known that EM1 is used to regulate the ICE regime, hence its speed is a control variable, but in terms of design of the control algorithm, it is equivalent to choosing the ICE speed ω_{ICE}, since they are kinematically related. Moreover, this choice presents an advantage that will be later discussed. The other control variable is the ICE torque T_{ICE}. In fact, the ICE operating point can be suitably decided at any instant, provided the mechanical and electrical limitations of the powertrains are always satisfied. The characteristic relations of the power-split transmission are here recalled for clarity:

$$\begin{cases} \omega_{ICE} = \dfrac{\big(\omega_{EM1} + K\omega_{ring}\big)}{(K+1)} \\ T_{EM1} = -\dfrac{T_{ICE}}{(K+1)}\eta_{planets-sun} \\ T_{ring} = \dfrac{K}{K+1}T_{ICE}\eta_{planets-ring} \end{cases} \tag{10}$$

Therefore, the system of equations (10) is used to derive the formula for P_{EM1} and P_{ring}. The angular speed ω_{ring} is equal to the driveshaft speed and it is related to the vehicle speed via the final-drive ratio and the wheel radius.

$$P_{EM1} = -\frac{T_{ICE}}{(K+1)}\eta_{planets-sun}\big[\omega_{ICE}(K+1) - K\omega_{ring}\big] \tag{11}$$

$$P_{ring} = T_{ring}\omega_{ring} = \frac{K}{K+1}T_{ICE}\eta_{planets-ring}\omega_{ring} \tag{12}$$

Finally, the previous relations are substituted into equation (9) to result into the instantaneous cost function employed in the ECMS algorithm.

The ECMS-based control algorithm evaluates the instantaneous cost function for different candidate control pairs $(\omega_{ICE}^i, T_{ICE}^i)$ which are selected from a pool of feasible solutions, which must satisfy several constraints. It is now easy to grasp the benefit of using ω_{ICE} in place of ω_{EM1} for the control variable: the power-split architecture of

interest has a clutch to ground the carrier of the planetary transmission when the ICE is shut-off, for example during the electric-drive mode. In this case $\omega_{ICE} = 0$ and $P_{ICE} = 0$, but ω_{EM1} would still rotate. Therefore, the use of ω_{ICE} as the second control variable allows to avoid the use of another control variable that should consider the clutch activation.

All the constraints are listed below. The torque limitations for both EM1 and EM2 are calculated at each instant by interpolation on the respective torque-speed maps: indeed, as the rotational speed (EM1) and torque (EM1, EM2) depend on the set ICE operating point, the EMs torque boundaries are calculated for all the possible power flows of the powertrain, defined by each candidate control pair. It is also assumed that the EM2 is correctly designed to sustain the vehicle speed range of the driving cycle ($\omega_{EM2} \in [\omega_{EM2,min}, \omega_{EM2,max}]$): anyway, this aspect was considered in the preliminary design phase:

1. ω_{ICE} s.t. $\omega_{ICE} \in [0, \dots, \omega_{ICE,max}]$
2. $T_{ICE}(\omega_{ICE}^i)$ s.t. $T_{ICE}(\omega_{ICE}^i) \in [T_{ICE}^{min}(\omega_{ICE}^i), \dots, T_{ICE}^{max}(\omega_{ICE}^i)]$
3. ω_{EM1} s.t. $\omega_{EM1} \in [\omega_{EM1,min}, \omega_{EM1,max}]$
4. $T_{EM1}(\omega_{EM1}^i)$ s.t. $T_{EM1}(\omega_{EM1}^i) \in [T_{EM1}^{min}(\omega_{EM1}^i), \dots, T_{EM1}^{max}(\omega_{EM1}^i)]$
5. $T_{EM2}(\omega_{EM2}^i)$ s.t. $T_{EM2}(\omega_{EM2}^i) \in [T_{EM2}^{min}(\omega_{EM2}^i), \dots, T_{EM2}^{max}(\omega_{EM2}^i)]$

Each candidate control pair must satisfy the power balance, given the power request by the driver:

$$P_{ICE} + P_{EM1} + P_{EM2} - P_{des} = 0 \tag{14}$$

It must be noted that in case of a braking event (i.e. $P_{des} < 0$), P_{des} is not set equal to the total requested braking power (which also includes the mechanical friction brakes' power demand), but only the regenerative braking power that can be actuated by EM2, as it is calculated by the RBS controller. Also, the battery charging and discharging power limitations influence the operating range of both EM1 and EM2, in fact the BMS logic may limit the power flow of EM1 and EM2 when they are working simultaneously. This aspect is taken care of at a lower level than the ECMS one as it was already explained for the RBC control strategy. Eventually, the cost function (equation 9) is calculated for the resulting admissible pairs $(\omega_{ICE}^i, T_{ICE}^i)$ and the optimal control pair is found $(\omega_{ICE}^{opt}, T_{ICE}^{opt})$. The control-strategy that has been described so far was implemented in Simulink.

A penalty function is added to avoid too high oscillation of the ICE power output and it is formulated with a quadratic function, explained in equation:

$$p\big(\Delta P_{ICE}(t)\big) = \gamma \left(\frac{P_{ICE}^i - P_{ICE}^{act}}{\Delta P_{ICE}^{adm}} \right)^{2t} \tag{16}$$

where γ is the weight factor (its order of magnitude is usually 10^3), P_{ICE}^{act} is the current ICE power output, ΔP_{ICE}^{adm} the admissible power deviation (it is not set higher than 10 kW per second), t is the order of the penalty term which has been set to 1. As indicated

by the superscript "i", a different value of the penalty is associated to each candidate control couple $(\omega_{ICE}^{i}, T_{ICE}^{i})$. In addition, also a constraint on the ICE state is implemented, which means that the ICE must continuously produce power for a minimum time interval: during this period of time, the control candidates which either have $\omega_{ICE}^{i} = 0$, or $T_{ICE}^{i} = 0$ are discarded from the pool of admissible control cadidates.

When, the objective is the reduction of the engine-out emissions, the ICE operating points should be moved towards the RCCI region. Consequently, a penalty on the NOx emissions is incorporated in the same fashion of the P2-parallel HEV control strategy [14].

$$p_1\big(NOx(t)\big) = \beta\left(\frac{|NOx_{min} - NOx(u(t),t)|}{NOx_{max} - NOx_{min}}\right)^{2r} \tag{17}$$

The calibration of the equivalence factor is a fundamental task in order to obtain the most convenient SoC trajectory:

$$s(SoC,t) = s_0\left(1 - \left(\frac{k_P\big(SoC(t) - SoC_{ref}\big)}{\Delta SoC_{norm}/2}\right)^{q}\right) \tag{18}$$

where s_0 is the constant equivalence factor, which is calibrated off-line for a driving cycle so that final SoC target is achieved. The term within the brackets is a penalty function based on battery SoC feedback signal, and the two parameters k_P and q can be tuned to adjust the severity of the penalty. $\Delta SoC_{norm} = 0.6 \pm 0.2$ is the desired SoC range. Due to this formulation of the equivalence factor, the ECMS-based algorithm is also named adaptive-ECMS.

The desired calibration is performed through iterative search. In addition, the weight factor of the penalty applied on NOx emissions, β, is to be calibrated to reduce as much as possible the NOx and soot engine-out emissions.

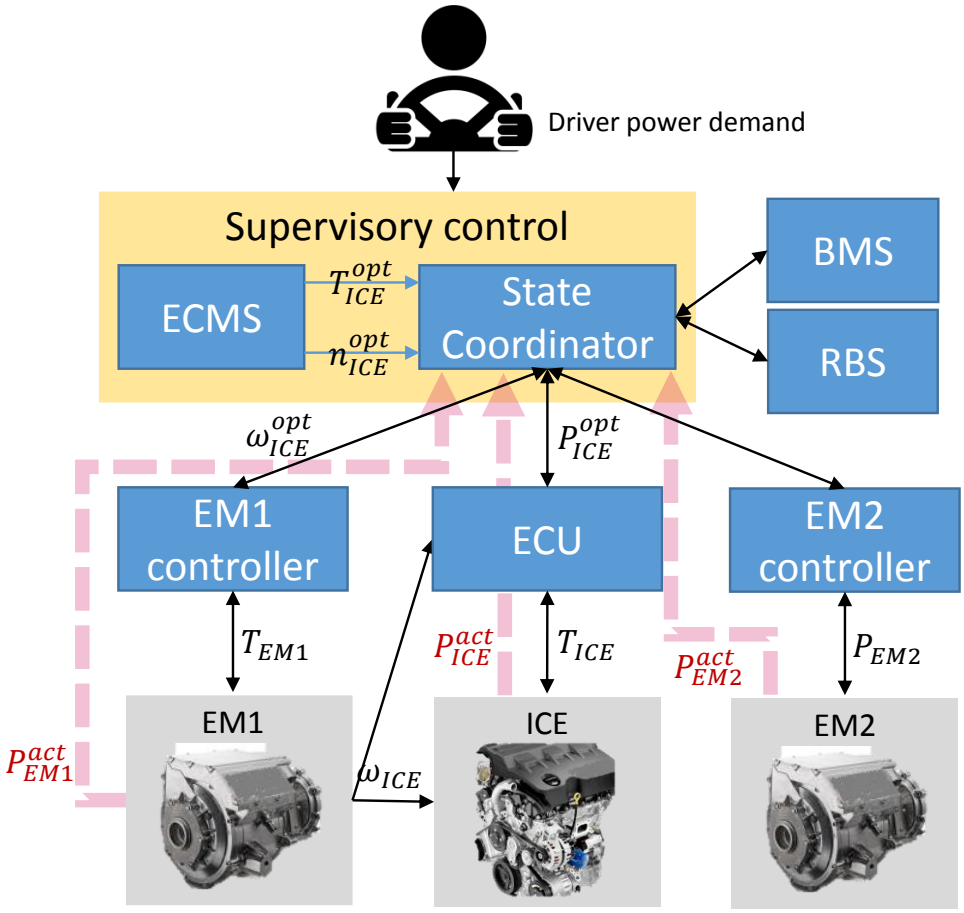

Figure 4 – Schematic of the control model structure of the power-split HEV.

Figure 4 shows a schematic of the powertrain control logic. Within the virtual supervisory energy management control unit, there can be found the ECMS optimization block and the state coordinator. The ECMS block produces the optimal desired torque and speed signals to control the ICE; these signals are sent to the supervisory state coordinator that has the task of coordinating the control signals to the actuators (EM1, EM2, ICE), depending on the state of the vehicle. In particular, when the ICE is switched off and the ECMS requests positive power to the ICE, the state coordinator has the task to first enter the "ICE start" state if the engine speed is below idle: in this way the EM1 is actuated so that it can drag the ICE up to the minimum required idle speed to enable the ICE fueling. Table 5 and Table 6 give an overview of the operative states and rules used to coordinate the powertrain.

Table 4. State Coordinator: main states of operation of the powertrain and actuation control signals. $\boldsymbol{T_{des}}$ – desired driver torque demand, $\boldsymbol{P_{des}}$ – desired driver power demand, $\boldsymbol{P_{frictBrake}}$ – mechanica frictionl brakes power, $\boldsymbol{P_{losses}}$ – estimated mechanical power losses of the transmission, $\boldsymbol{P_{ring}}$ – ring output power, $\boldsymbol{P_{ICE}^{idle}}$ - ICE power output at idle.

State	EM1 torque	EM2 power	ICE power	ICE speed
Vehicle Stop	0	0	0	0

EV drive	$\max_{T_{des}>0}[(T_{des} - T_{EM2}), 0]$ $\min_{T_{des}<0}[(T_{des} - T_{EM2}), 0]$	$P_{des} - P_{frictBrake} + P_{losses}$	0	0
ICE start	T_{EM1}	$P_{des} - P_{frictBrake} + P_{losses}$	P_{ICE}^{idle}	ω_{ICE}^{idle}
HEV drive	T_{EM1}	$P_{des} - P_{ring} - P_{frictBrake} + P_{losses}$	$P_{ICE}^{opt} = \omega_{ICE}^{opt} * T_{ICE}^{opt}$	ω_{ICE}^{opt}

Table 5. State Coordinator: description of the conditions for the transitions between the states.

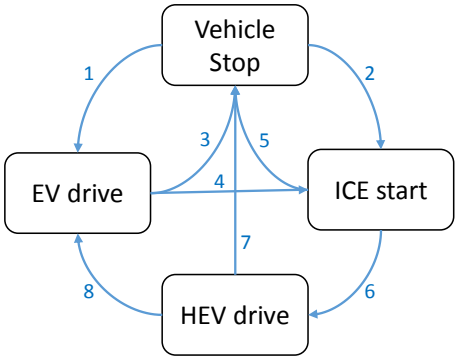

State Coordinator		States transitions descriptions
1	Vehicle Stop – EV drive	$v_{veh,des} > 0$ AND $P_{ICE}^{opt} = 0$
2	Vehicle Stop – ICE start	$v_{veh,des} > 0$ AND $P_{ICE}^{opt} > 0$ AND $\omega_{ICE}^{act} < \omega_{ICE}^{idle}$
3	EV drive – Vehicle Stop	$v_{veh,des} = 0$
4	EV drive – ICE start	$v_{veh,des} > 0$ AND $P_{ICE}^{opt} > 0$ AND $\omega_{ICE}^{act} < \omega_{ICE}^{idle}$
5	ICE start – Vehicle Stop	$v_{veh,des} = 0$
6	ICE start – HEV drive	$v_{veh,des} > 0$ AND $P_{ICE}^{opt} > 0$ AND $\omega_{ICE}^{act} > \omega_{ICE}^{idle}$
7	HEV drive – Vehicle Stop	$v_{veh,des} = 0$
8	HEV drive – EV drive	$v_{veh,des} > 0$ AND $P_{ICE}^{opt} = 0$

3. Results

3.1. Vehicle components sizing

The DP algorithm was used together with a DoE analysis to sweep through the design parameters of interest to look for the optimal sizing of the powertrain components. Furthermore, the design procedure through DP was split in two phases, given the high number of parameters: the first phase involves a sweep through K and τ_{FD}; the second phase uses the best solution of the first phase and explores the combinations of $f_{scale,EM1}$, $f_{scale,EM2}$ and N_p. The optimal design study is performed for both the fuel-economy than emissions-reduction cases.

As explained in section 2.3, the optimal control operation of the power-split HEV is enacted through the speed and the torque of the ICE. The distribution of the ICE operating points for the best solutions of the fuel-economy and emissions-reduction scenarios can be seen in Figure 5: the minimum BSFC and BSNOx lines are also displayed to highlight the fact that forcing the ICE operation onto those lines would unlikely lead to optimal results.

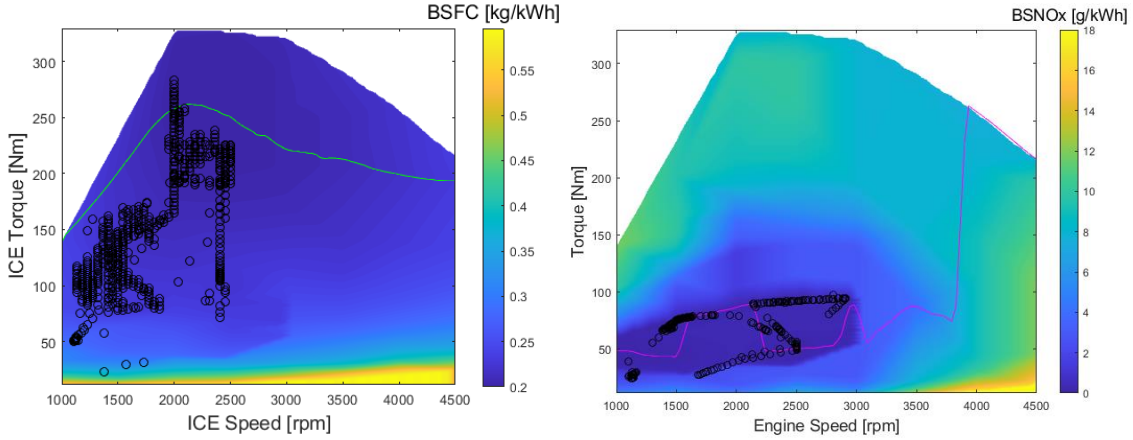

(a) (b)

Figure 5 – ICE operating points distribution for the best solutions found in the first optimization phase: (a) fuel-economy optimization; (b) emissions-reduction optimization.

The results of the first optimization phase are reported in Figure 6 (fuel economy optimization) and Figure 7 (emissions-reduction). In the latter, the emission levels for NOx are less than half the Euro 6 limit (**¡Error! No se encuentra el origen de la referencia.** 6b). Furthermore, for the fuel-economy optimization, the soot emissions maximum levels were 2.6×10^{-3} g/km, but with the emissions-reduction strategy they reached ultra-low levels below 4×10^{-4} g/km. Given that the emissions levels were compliant with the regulations for all the studied cases with DoE, the selection of the optimal configuration for the emissions-reduction scenario was based on the fuel consumption (Figure 7a).

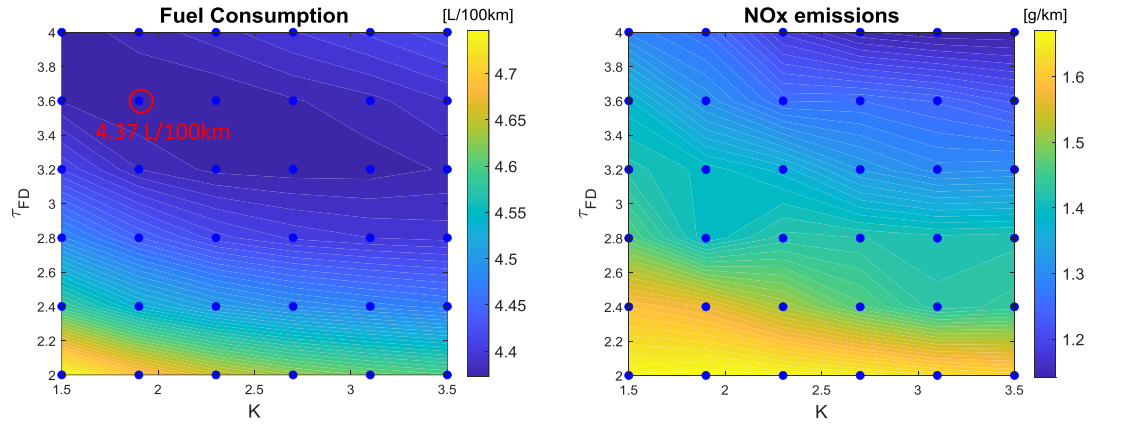

(a) (b)

Figure 6 – DoE analysis results of the 1st phase of the fuel-economy optimal design procedure with dynamic programming. The best solution is encircled in red.

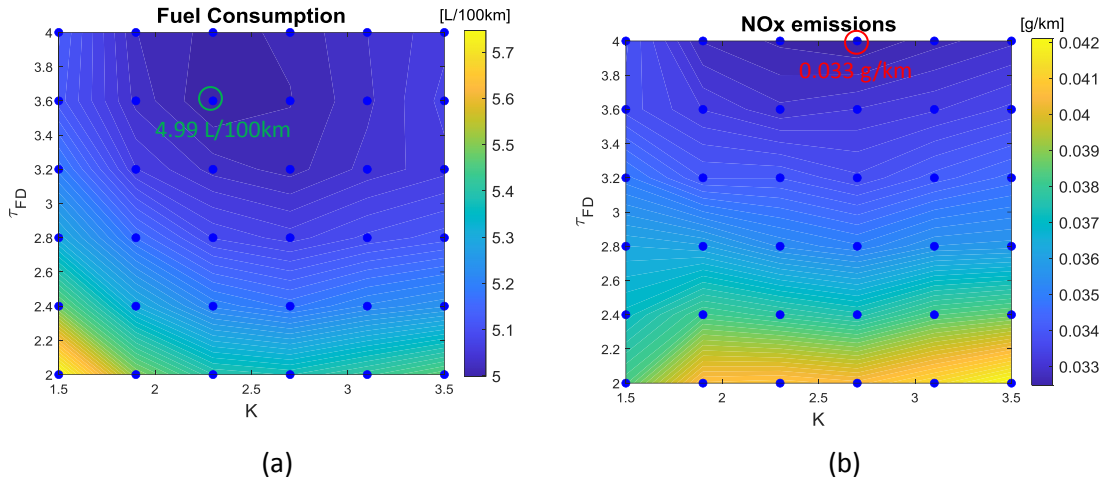

(a) (b)

Figure 7 – DoE analysis results of the 1st phase of the emissions reduction optimal design procedure with dynamic programming. The best NOx emissions solution is encircled in red; the best fuel-economy solution is encircled in green.

To summarize the results, Table 4.6 reports the best configurations of (K, τ_{FD}) for the fuel-economy and emissions-reduction optimal strategies.

Table 6. Best setup of planetary gear-train and final drive transmission ratios, determined through DoE analysis for the fuel economy and emissions-reduction strategies.

Free control variables in DP	Fuel-economy optimization	Engine-out emissions minimization
T_{ICE}, n_{ICE}	$K = 1.9$ $\tau_{FD} = 3.6$	$K = 2.3$ $\tau_{FD} = 3.6$

It must be noted (Figure 6a) that in the fuel-economy optimization, the fuel consumption variation for different values of K, at the resultant best τ_{FD}, is almost 1 %. Also, the fuel consumption for the nearest explored configurations of τ_{FD} increases by 1 %. Moreover, both parameters influence the vehicle performance and in particular higher values of τ_{FD} improve the vehicle hybrid boost mode at the low vehicle speeds, even though K has a smaller effect. However, too high values of τ_{FD} decrease the maximum vehicle speed. The vehicle hybridization with the power-split architecture is less capable of improving the vehicle performances as it occurred with the P2-parallel one. Even though this is not the objective of this work, the vehicle baseline characteristics should not be excessively altered (i.e. deteriorated). Furthermore, it can be noted from Figure 8, that the HEV powertrain under study cannot rival the conventional ICE-powered vehicle at the low speeds, but this is due to the high multiplication ratio of the ICE torque output to the wheels, given by the combined effect of the OEM transmission ratio of the first gear of the six-speed gearbox and the fixed final drive transmission ratio. For this reason, the choice of the best configuration for the planetary transmission ratio and the final drive ratio in this scenario is made by also

considering this aspect (i.e. torque capability) and to reduce the gap with the baseline ICE-powered platform. At last, τ_{FD} is set to 3.6, while K to 2.7. The fuel consumption corresponding to this case is 4.38 L/100km, that is 0.45 % higher with respect to the best solution found with the DoE study. In this way, the same setup can also be applied for the emissions-reduction strategy and also in this case there is a marginal increase in fuel consumption (less than 1 %), the engine-out emissions are anyway still very good.

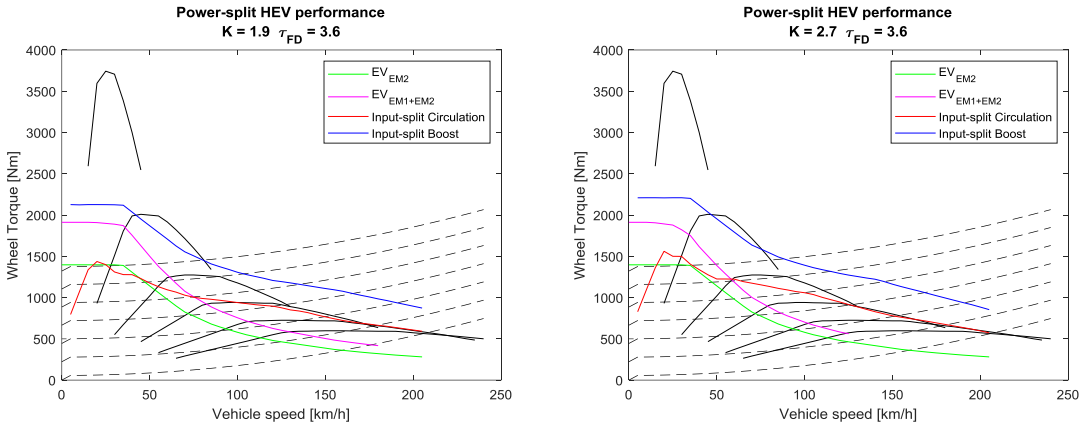

Figure 8 – Power-split HEV performance map: (a) $\boldsymbol{K}$ and $\boldsymbol{\tau_{FD}}$ resulting from the fuel-economy DoE optimization; (b) upgrade of $\boldsymbol{K}$ and $\boldsymbol{\tau_{FD}}$ to improve the vehicle torque capability. The black continuous curves represent the tractive torque output of the baseline ICE-powered vehicle, equipped with a six-speed transmission.

The second phase of the optimal sizing procedure is to choose EM1 and EM2 and the battery size (the number of parallel connections N_p is the only design variable). As explained in the previous paragraph, the two strategies are now tested for fixed values of K and τ_{FD}, set to 2.7 and 3.6, respectively.

Figure 9 reports the results for the fuel-economy strategy. A power rating below 38 kW for EM2 is not enough to satisfy the power demand at the wheels. Overall, there is a maximum variation of fuel consumption of about 2 % for the different sizes of EM1 and EM2, and the best solution can be found when the sizes of EM1 and EM2 are smaller than the original ones. However, as previously highlighted, the vehicle performances should not be excessively altered and for this reason the size of EM2 is maintained equal to the baseline value. Furthermore, the effect of increasing the number of parallel connections for the battery pack improves the overall trend: it appears to have a positive effect on the charge power voltage limitation (19) hence it allows greater charging power input to the battery.

$$P_{charge,Vmax} = OCV\left(\frac{OCV - V_{max,cutoff}}{R_0}\right) - R_0\left(\frac{OCV - V_{max,cutoff}}{R_0}\right)^2 \qquad (19)$$

In fact, by increasing the number of parallel cells, the internal resistance of the battery decreases. Figure 10 better highlights this behavior: the zoomed plot shows one event during which the extended charging power limitation on voltage allows more power to be input to the battery when 4 parallel cells are used in place of 3. At last, the bigger battery pack allows on average almost 9 % more charging power. However,

compared to the first phase of the design procedure, if the number of parallel cells is increased to 4 and the sizes of EM1 and EM2 are not changed, there is an overall improvement in fuel consumption that is lower than 1% (Figure 9). The same result also applies if the size of EM1 is reduced as suggested by the contour plots. In truth, the choice for a larger number of parallel connections would consider battery ageing effects as well, but this aspect is not accounted for in this work. For this reason, it was finally chosen to maintain the original sizes of these two components.

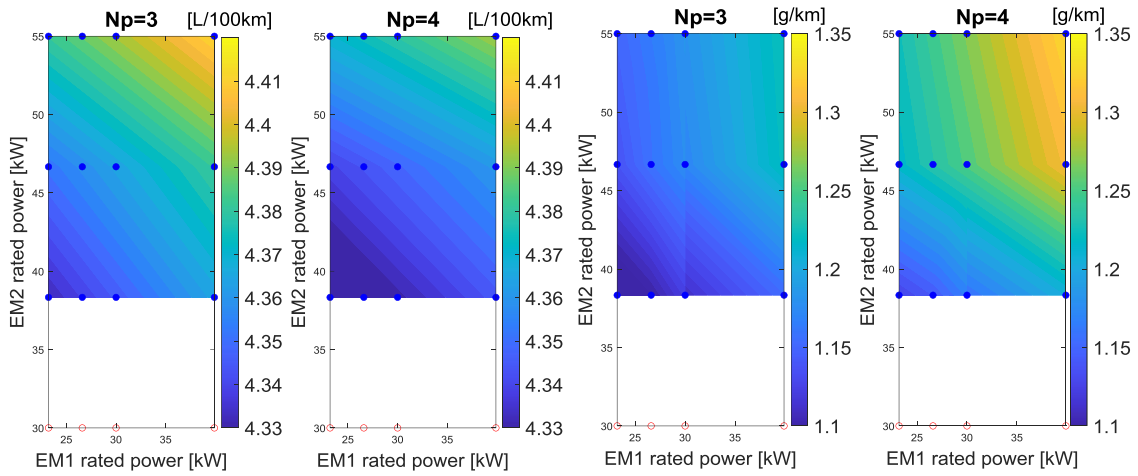

Figure 9 – DoE analysis results of the 2nd phase of the fuel-economy optimal design procedure with dynamic programming. (a) Fuel consumption; (b) NOx emissions. All the dots represent the analyzed cases: blue dots are feasible; the red ones are infeasible.

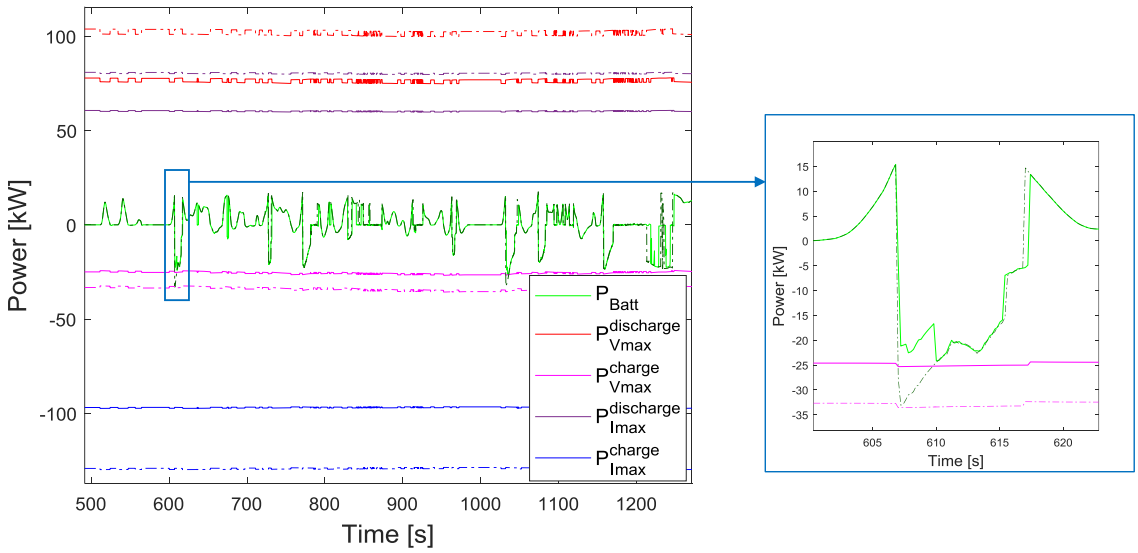

Figure 10 - Battery power limitation signals in two situations: the continuous and dashed lines refer to a number of parallel cells equal to 3, and 4 respectively. The same color is used to plot similar quantities.

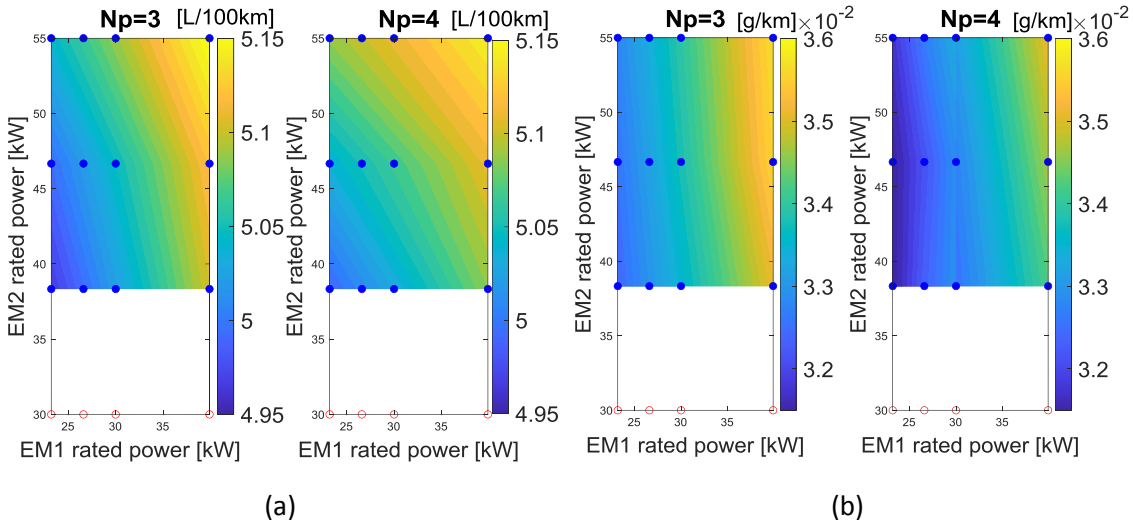

Figure 11 – DoE analysis results of the 2nd phase of the emissions-oriented optimal design procedure for $\boldsymbol{\beta = 1000}$. (a) Fuel consumption; (b) NOx emissions. All the dots represent the analyzed cases: blue dots are feasible; the red ones are infeasible.

In the emissions-reduction case the results are very similar to those obtained with the first phase of the design procedure (NOx = 0.032 g/km). Both the sizes of EM2 and of the battery pack (i.e. the number of parallel cells) have a negligible effect on the fuel consumption and emissions. The optimal design would prescribe a reduced size for EM1 since the power output by the ICE which can be absorbed by the EM1 is constrained in the RCCI region.

In general, it can be noticed that the Euro VI limits are amply satisfied (soot emissions score at maximum 2.4*10-4 g/km). For the same emissions-reduction scenario, the P2-parallel HEV scored a fuel consumption equal to 4.72 L/100km while NOx emissions were equal to 0.057 g/km (soot emissions 6*10-4 g/km) [14]. For this reason, the penalty on the NOx emissions could be softened to improve a little bit the fuel consumption. Hence, after some iterations it was found that a good compromise is achieved when the DP penalty factor for NOx engine-out emissions β is set to 100: the new results of the DoE analysis are reported in Figure 12. With a lower NOx penalty, the fuel consumption is equal to 4.82 L/100 km, instead of 5.1 L/100 km, when EM1 and EM2 are set to 30 and 50 kW respectively (different battery sizes do not change the result significantly).

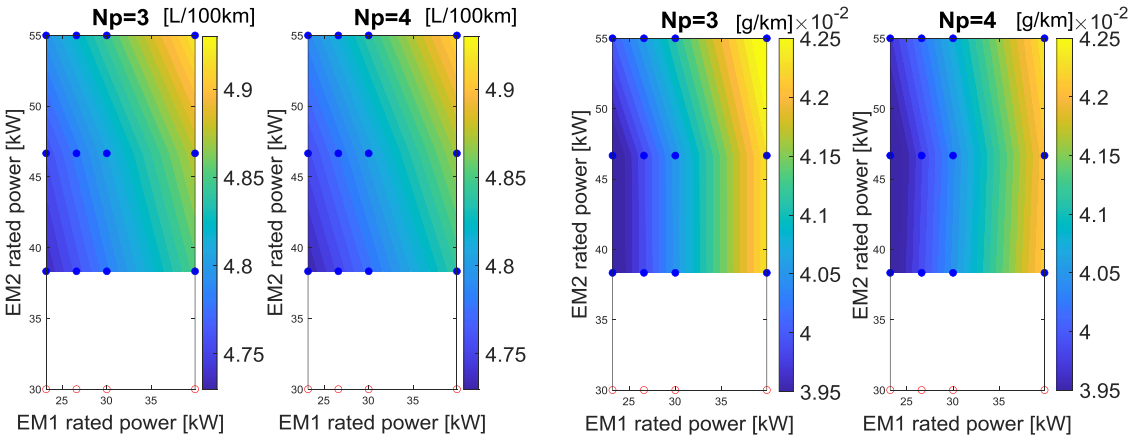

(a) (b)

Figure 12 – DoE analysis results of the 2nd phase of the emissions-oriented optimal design procedure for $\boldsymbol{\beta = 100}$. ICE speed and torque are free control variables. (a) Fuel consumption; (b) NOx emissions. All the dots represent the analyzed cases: blue dots are feasible; the red ones are infeasible.

3.2. Operation optimization with on-line energy management strategies

This section assesses the problem of the on-line control for a power-split HEV equipped with the dual-mode RCCI-CDC engine. The analysis is equivalent to that made for the P2-parallel HEV: the RBC and the aECMS are tested. Both control approaches are employed to exploit the best fuel-economy capability of the vehicle and the best emissions-reduction potential. The power-split HEV powertrain presents more challenges compared to the P2-parallel HEV, but especially the sub-optimal strategy (aECMS) offers an analytical way to tackle the control problem, finally proving to be superior to RBC. Furthermore, the possibility to gain both the advantages of the parallel and series HEV architectures, stimulates the interest to investigate whether under real-time operation the power-split HEV is able to effectively reduce the engine-out NOx and soot emissions by operating with improved efficacy in the RCCI region of the dual-mode RCCI-CDC engine.

3.2.1. Rule-Based Control strategy

The power-to-speed curve is a fundamental piece of information for the current strategy because it allows to set the operation point of the ICE at any instant: it was built by considering the results obtained with DP (Figure 5a). The power-to-speed curves are displayed in Figure 13. The fuel-economy oriented strategy is performed by implementing the blue curve, which is compared against the minimum BSFC curve (dashed blue curve). Since the same design of the control strategy is also used to try to minimize the NOx (and soot) engine-out emissions, the ICE should be able to work in the RCCI region. For this reason, another power-to-speed curve was created for this case (magenta curve). The slight deviation between the power-to-speed curve used for the emissions-reduction strategy and the minimum BSNOx curve can be neglected since the RCCI region is limited under 3000 rpm (Figure 1).

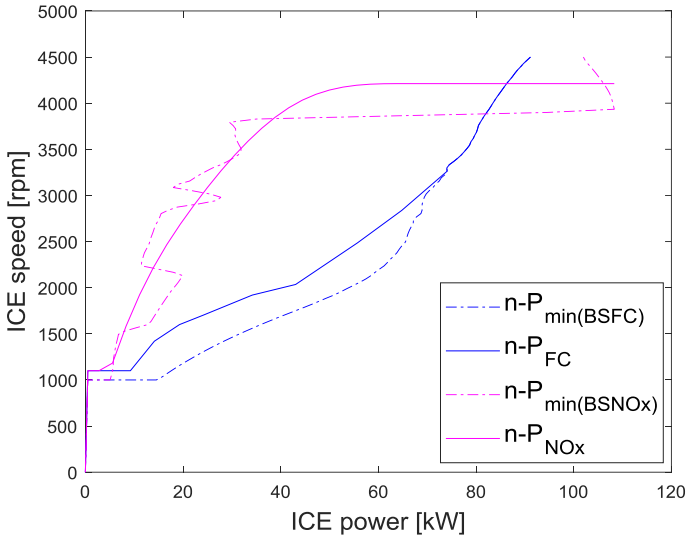

Figure 13 – Power-to-speed curve for the RBC strategies of the power-split HEV. n-P_{FC} and n-P_{NOx} are adopted for the fuel-economy oriented and emissions-reduction oriented strategies respectively.

The values of all the parameters which have been implemented in the control strategy are calibrated via a genetic algorithm in GT-Suite: the target functions are the minimization of the fuel consumption and the minimization of the engine-out NOx emissions. Furthermore, the deviation between the final and target SoC values should not exceed 1%, as well as the upper and lower SoC limits should not be violated. The calibration parameters for the two control strategies are reported in Table 6.6.

Table 7. Best calibration of the control parameters of the RBC strategies.

RBC parameters	P_{ICE}^{min}	P_{ICE}^{max}	SoC_{min}	$SoC_{charge,max}$	$v_{EM2,max}$	Δt_{min}^{ICE}	K_I^{SoC}	K_P^{SoC}
RBC Fuel oriented	21.3	-	0.538	0.71	50	10	46.144	34.308
RBC emissions oriented	19.5	24.1	0.542	0.689	0	0	20.861	5.638

At last, the results are presented in Figure **14** 14: the plots show the behavior of the main powertrain components when operated under the RBC strategy in the two scenarios.

Fuel-Economy oriented RBC NOx emissions-oriented RBC

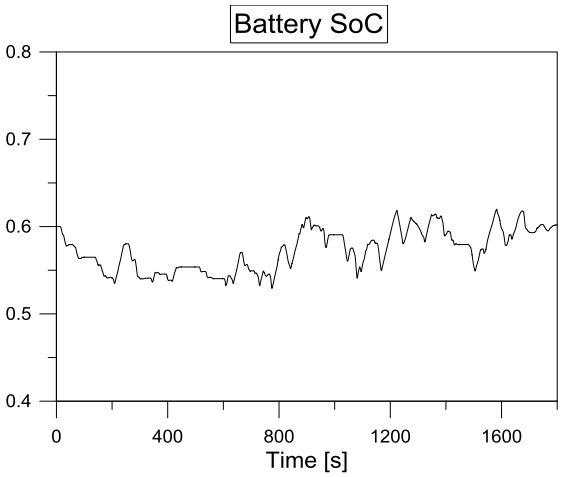
Battery SoC
0.8
0.7
0.6
0.5
0.4
0
400
800
1200
1600
Time [s]

(a)

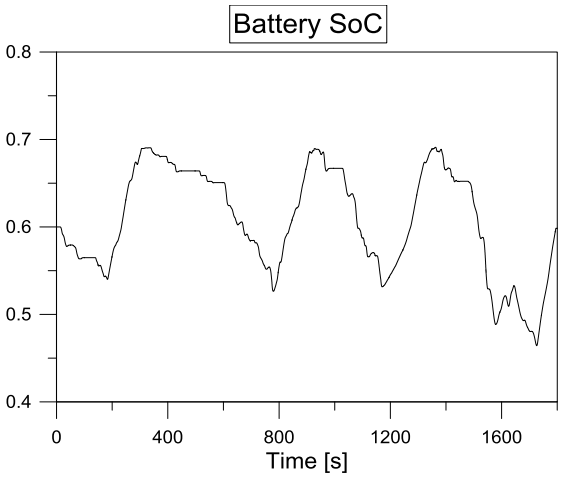
Battery SoC
0.8
0.7
0.6
0.5
0.4
0
400
800
1200
1600
Time [s]

(b)

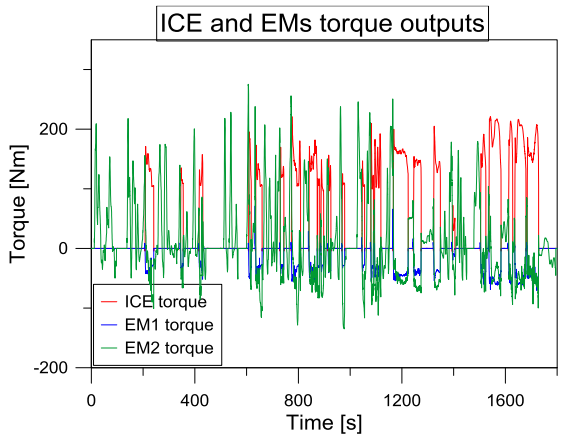
ICE and EMs torque outputs
Torque [Nm]
200
0
-200
ICE torque
EM1 torque
EM2 torque
0
400
800
1200
1600
Time [s]

(c)

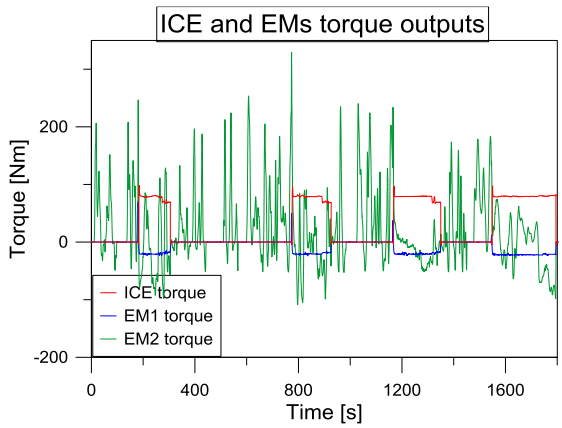
ICE and EMs torque outputs
Torque [Nm]
200
0
-200
ICE torque
EM1 torque
EM2 torque
0
400
800
1200
1600
Time [s]

(d)

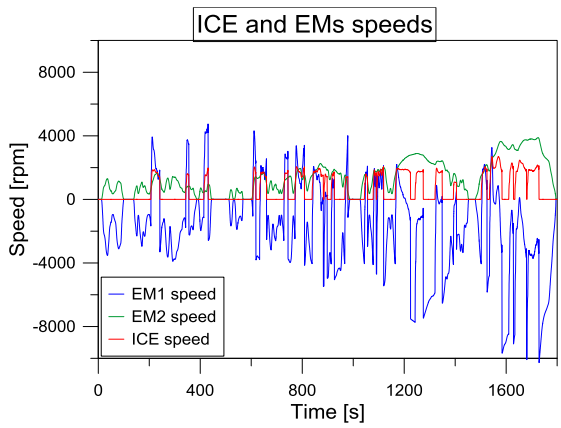
ICE and EMs speeds
Speed [rpm]
8000
4000
0
-4000
-8000
EM1 speed
EM2 speed
ICE speed
0
400
800
1200
1600
Time [s]

(e)

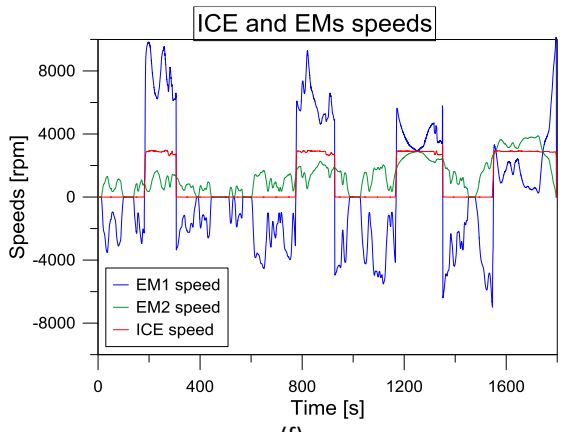
ICE and EMs speeds
Speeds [rpm]
8000
4000
0
-4000
-8000
EM1 speed
EM2 speed
ICE speed
0
400
800
1200
1600
Time [s]

(f)

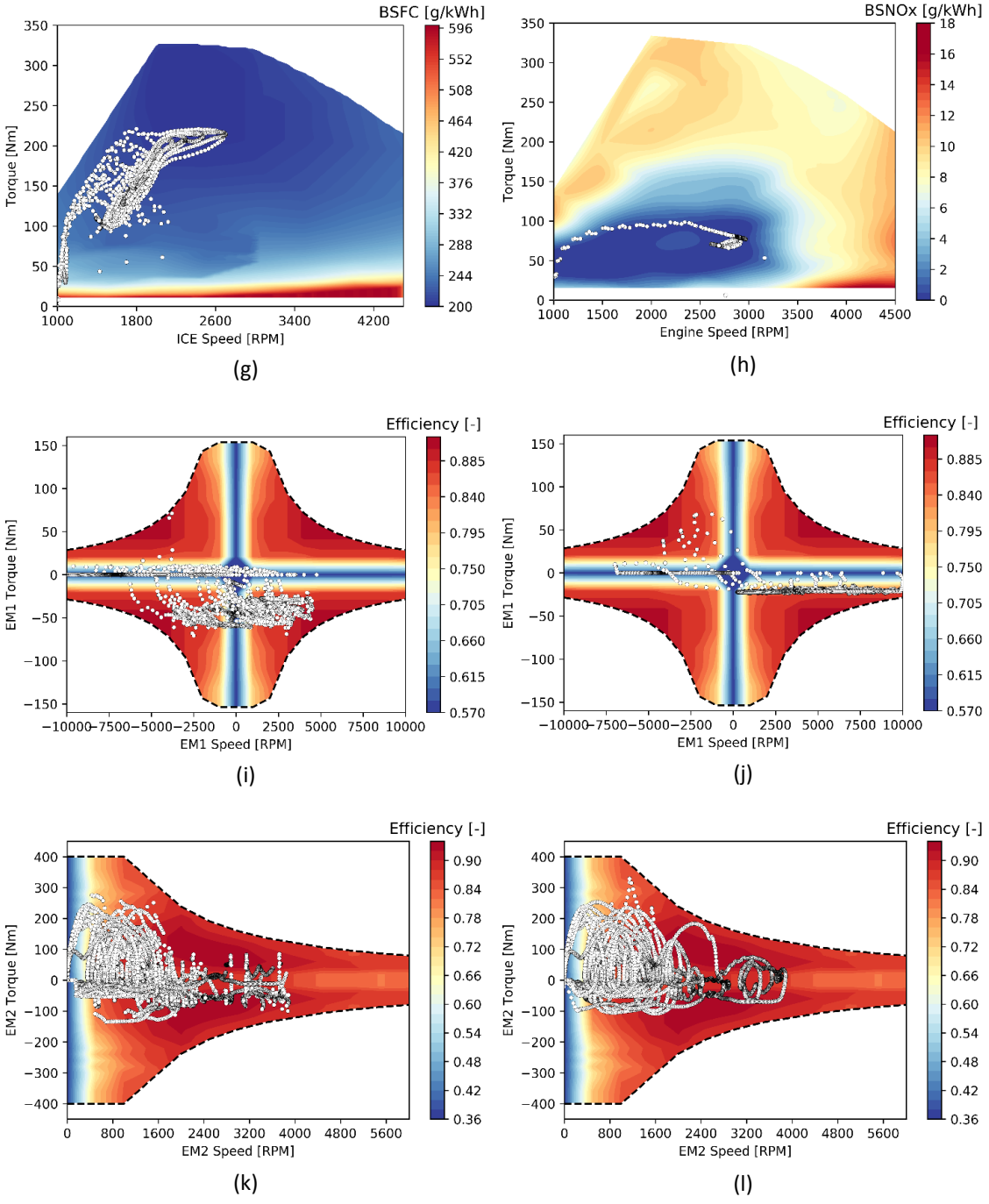

Figure 14 – Characteristic plots of the optimal calibration for the RBC fuel-economy-oriented strategy (left column) and RBC emissions-oriented strategy (right column) for the power-split HEV.

For the fuel-economy oriented strategy the first thing to be noticed is the narrower SoC trajectory compared to the one given by DP (Figure 14a): the battery SoC level deviates at maximum 0.05 from the reference value. The battery is discharged only during EV drive (Figure 14c), while when in “HEV drive” mode the designed strategy makes the ICE operating at high loads, so that its output is usually greater than the traction power request and promptly recharges the battery. The EM2 is used under input-split boost mode, but it mostly operates in re-circulation mode to absorb the extra ICE power. The distribution of points of the ICE (Figure 14g) presents a major cluster due to the implementation of the power-to-speed curve that has the purpose

to control the ICE at an improved tank-to-wheel efficiency, according to the results given by DP analysis.

The RBC emissions-reduction strategy performs very differently from DP. In fact, there are still parts of the driving cycle where the engine is shut-off and the vehicle is driven in "EV drive" mode. Then, as the SoC reaches the set minimum SoC level, the ICE is switched on and it continuously operates for at least 80 s. The distribution of the ICE operating points is spread out at the upper edge of the RCCI region. Its speed and torque output are kept almost steady (Figure 14d and Figure 14f), quite resembling the behavior of the series HEV. Although, the final engine-out NOx emissions are close to being compliant with the Euro VI legislation, the fuel consumption is even higher than for the conventional vehicle. The clear difference between the obtained SoC trajectory and optimal one achieved with DP gives evidence that the powertrain is not being operated in the best possible way, further indicating that there is much room for improvement for the design of the RBC strategy.

3.2.2. Adaptive Equivalent Consumption Minimization Strategy

The results obtained from the design and calibration of the ECMS-based control algorithm, are presented for the best fuel-economy and emissions-reduction cases. Also, the values of the main calibration parameters are reported in Table 8.

Table 8. Calibration parameters of the control strategies based on the a-ECMS algorithm.

	Fuel-economy strategy	NOx-emissions-oriented strategy
Constant equivalence factor s_0	2.34	2.9
Proportional factor of SoC adaptation K_p	0.4	0.2
NOx penalty weight factor β	0	$3.0*10^6$
NOx penalty exponent multiplier r	1	1
ICE power variation penalty weight factor	5000	5000
ICE power variation penalty exponent multiplier t	1	1

The most significant results for the powertrain operation under the a-ECMS control strategy are displayed in Figure 15. It is interesting to note how the operating points are clustered when the objective of the ECMS algorithm is to minimize fuel consumption (Figure 15g): the distribution resembles the one obtained with DP, hence the operating points are close to the minimum BSFC line, but do not exactly match it because the tank-to-wheel efficiency may not be maximized there. On the other hand, the main differences are: operating points falling in the highest load region (i.e. peak torque $\sim$ 300 Nm); higher density of operating points in the lower efficiency region of the engine map (ICE torque and speed less than 100 Nm and 3000 rpm respectively). This behavior could not be easily corrected despite the calibration effort of the ECMS parameters, together with the design of the penalty functions to smoothen the ICE power output.

Anyway, in terms of fuel consumption the ECMS is worser than DP by 5 %, which is a reasonable deviation because ECMS is not a predictive control strategy and the algorithm only implements an adaptation of the equivalence factor based on the feedback battery SoC signal.

Figure 15**¡Error! No se encuentra el origen de la referencia.**h reports the ICE operating points on the BSNOx map when the supervisory control strategy is oriented to minimizing the engine-out NOx emissions. The operating points appear to cluster within the RCCI region. Also, they distribute at the top boundary of this region to enhance the ICE power output, which is severely reduced. In comparison to the P2-parallel HEV, since the EM coupled to the wheels has a greater torque/power capability, and since the ICE is decoupled from the vehicle dynamics, it is possible to a have a tighter control of the ICE regime: EM2 can compensate at any time for the power output requested at the wheels, while EM1 sets the most convenient ICE speed.

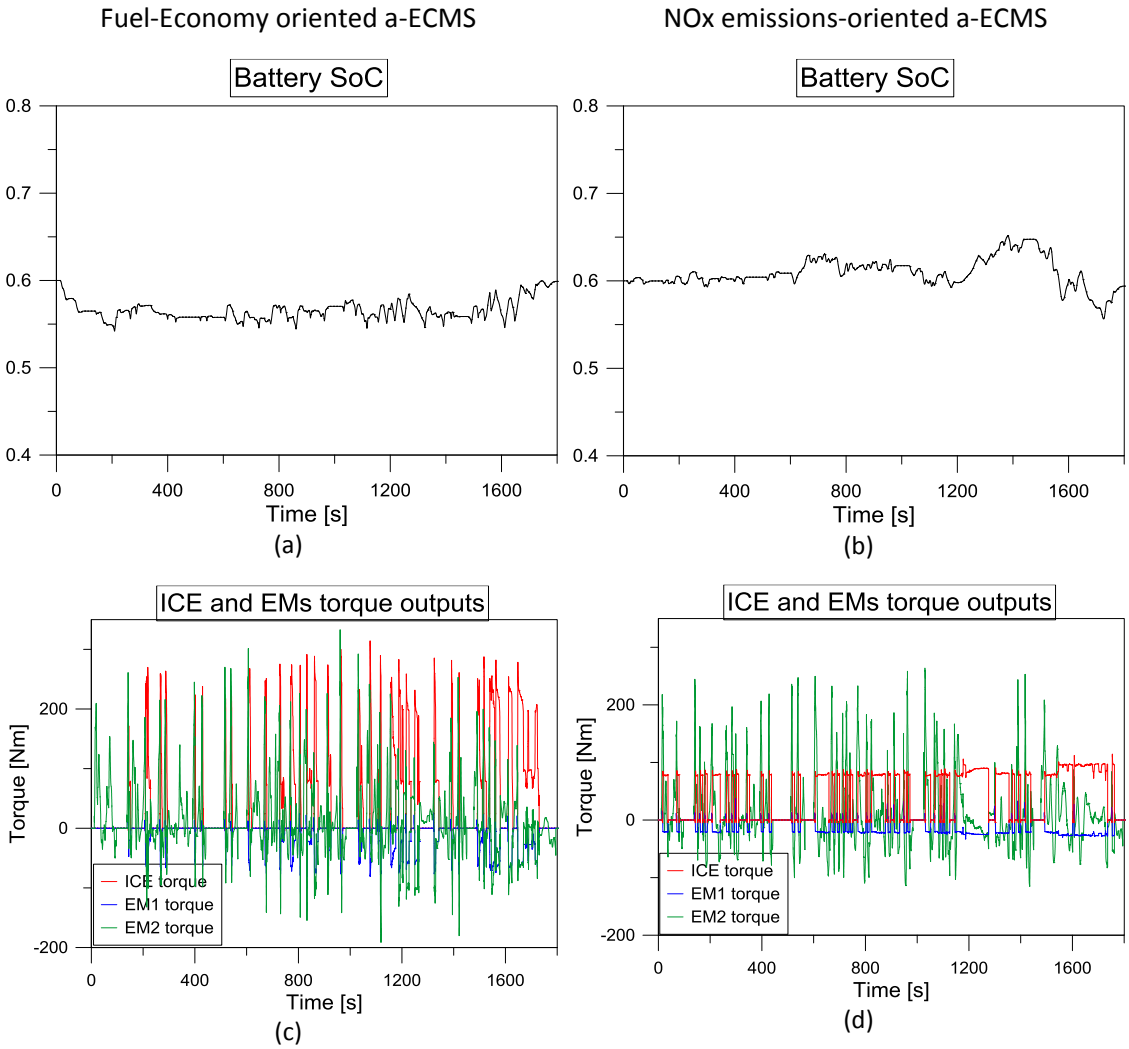

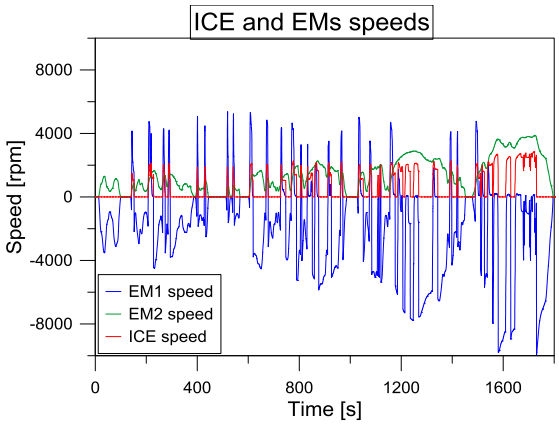
ICE and EMs speeds
Speed [rpm]
Time [s]
EM1 speed
EM2 speed
ICE speed

(e)

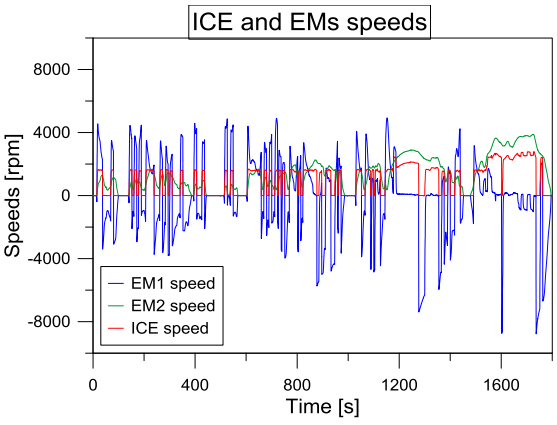
ICE and EMs speeds
Speeds [rpm]
Time [s]
EM1 speed
EM2 speed
ICE speed

(f)

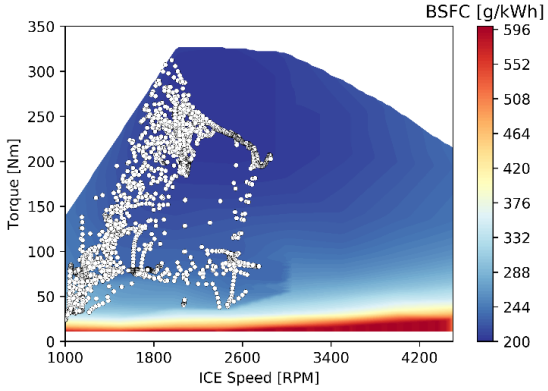
BSFC [g/kWh]
Torque [Nm]
ICE Speed [RPM]

(g)

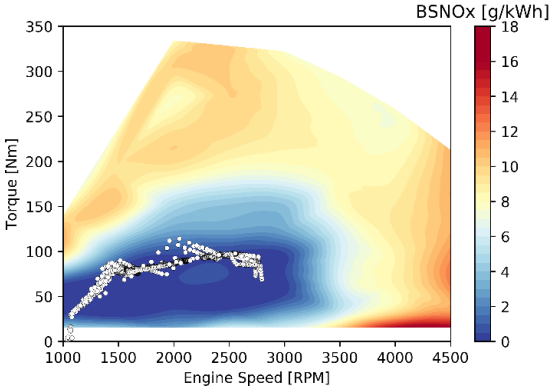
BSNOx [g/kWh]
Torque [Nm]
Engine Speed [RPM]

(h)

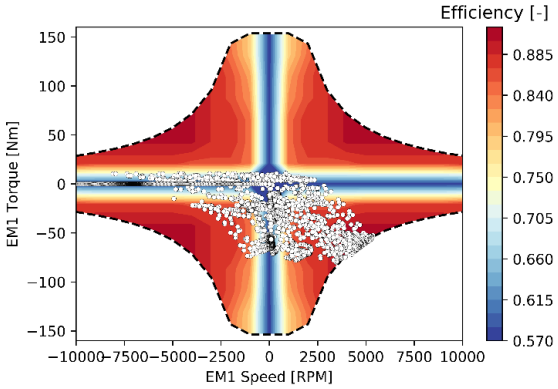
Efficiency [-]
EM1 Torque [Nm]
EM1 Speed [RPM]

(i)

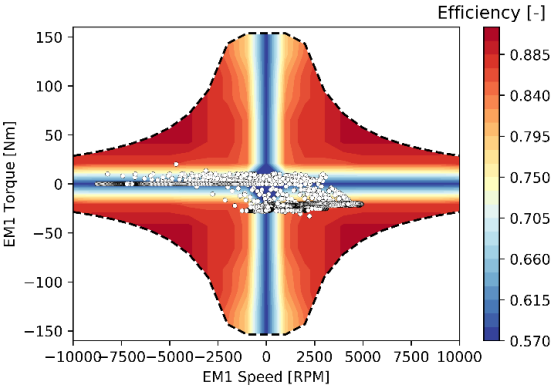
Efficiency [-]
EM1 Torque [Nm]
EM1 Speed [RPM]

(j)

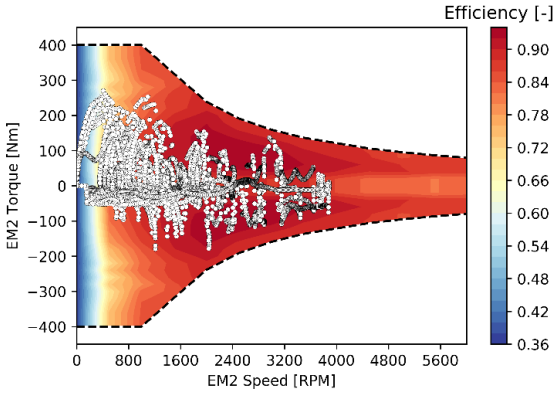
Efficiency [-]
EM2 Torque [Nm]
EM2 Speed [RPM]

(k)

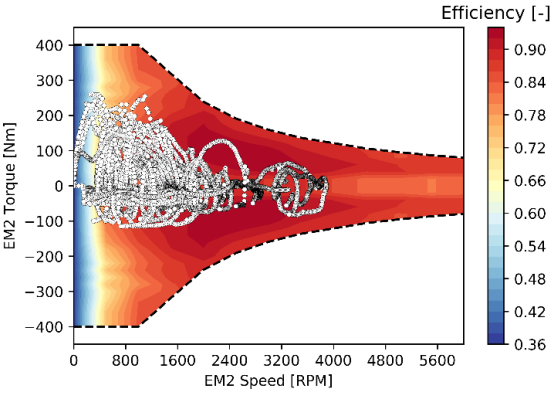
Efficiency [-]
EM2 Torque [Nm]
EM2 Speed [RPM]

(l)

Figure 15 – Characteristic plots of the a-ECMS fuel-economy-oriented strategy (left column) and a-ECMS emissions-oriented strategy (right column) for the power-split HEV.

The fact that the torque output of the ICE is reduced also reflects on the operation of EM1 and EM2. Due to the transmission ratio of the planetary geartrain, the torque produced in generator mode by EM1 is very low (Figure 15c): the distribution of these points is mostly concentrated in the low efficiency region of the EM1 map. This implies that the part of ICE power which is absorbed by EM1 undergoes a quite inefficient energy transformation with an average loss of 30%. Even though this issue was also seen in the analysis made with DP, it suggests that in the end the power-split architecture may result less efficient than the P2-parallel one to operate the emissions-reduction strategy, despite it is capable of a better control than the latter.

The EM2 exhibits a quite different behavior when operated under the emissions-reduction strategy: comparing 15c and 15d, it can be seen that EM2 operates most of the time in input-split boost mode and less in recirculation mode. Of course, this is due to the need to complement the reduced power output of the ICE as it is forced to work in the RCC region of the map, but even if this observation may seem trivial it actually indicates that an adequate size of EM2 is necessary to satisfy the power demand at the wheels even for more challenging drives than the WLTC. In this situation, the operating points of EM2 (Figure 15l) are distributed more or less in a similar fashion than in the fuel-economy case (Figure 15k).

At last, a final emphasis on the battery SoC trajectories shows that the two strategies have an opposite way of operating the powertrain. While the first one (Figure 15a) readily discharges the battery to favor pure electrical driving (the first 120 s are run only via the EM2), the second one (Figure 15b) switches on the ICE much sooner. The fuel-economy strategy uses the ICE to refurbish the battery energy content after it has been used and it mostly operates at the medium-high loads to improve the efficiency; the emissions-reduction strategy switches on the ICE in advance so that when the requested torque is greater than the admissible ICE torque for operating in the RCCI region, the EM2 can be activated. Furthermore, the SoC deviation is smaller than DP, but again this reflects the fact the ECMS does not provide a global optimal solution: while DP optimal SoC trajectory is unique, the solution obtained with ECMS may be one of many solutions, where the number of feasible solutions depends on the design of the control algorithm, but also on the calibration of the control parameters.

Table 9 gives a conclusive outlook of the fuel consumption and main engine-out emissions that are achieved with the power-split HEV controlled via the fuel-economy and the emissions-reduction control strategies.

Table 9. Results of the best fuel-economy calibration of the RBC and a-ECMS control strategies, compared with the baseline no-hybrid platforms and the results obtained with DP. The percentage relative deviations are calculated with respect to the CDC no-hybrid vehicle. *Euro 6 NOx limits for CI is 0.080 g/km and Euro 6 Soot is 0.0045 g/km.

Platform	Hybrid Control Strategy	Fuel Consumption	Relative Fuel Consumption difference	NOx Emissions	Relative NOx difference	Soot Emissions	Relative Soot difference
Unit	-	[L/100km]	[%]	[g/km]	[%]	[mg/km]	[%]
No-hybrid CDC	-	5.65	-	0.48	-	11.0	-
No-hybrid CDC + RCCI	-	5.73	+ 1.4	0.31	- 36.3	4.0	- 60
Power-split HEV CDC+RCCI	DP - FC	4.38	- 22.5	1.27	+ 164.4	2.5	- 77.3
Power-split HEV CDC + RCCI	DP - NOx	4.83	- 14.5	0.04	- 91.5	0.2	- 98
Power-split HEV CDC + RCCI	RBC - FC	4.78	- 15.4	1.20	+ 150	3.5	- 68.2
Power-split HEV CDC + RCCI	RBC - NOx	5.97	+ 5.7	0.07	- 82.5	0.4	- 96.3
Power-split HEV CDC + RCCI	aECMS - FC	4.66	- 17.5	1.40	+ 192.9	2.4	- 78.2
Power-split HEV CDC +RCCI	aECMS - NOx	5.37	- 4.9	0.06	- 86.3	1.1	- 90

*Marked in red underline the cases that exceed the No-Hybrid CDC fuel consumption or in terms of emissions exceed the Euro 6 limits.

4. Conclusions

This work has investigated the power-split HEV concept and its performance when equipped with the dual-mode RCCI-CDC engine. The power-split HEV is among the most diffused powertrain's architectures and it allows to encompass the advantages of both the parallel and series HEV architectures, such as the capability of driving the vehicle through the ICE and EMs in parallel, as well as to decouple the ICE from the wheel dynamics. However, this comes at the expense of an increased complication due to the implementation of the planetary geartrain and an additional EM.

Similarly, to the P2-parallel HEV, the a-ECMS control strategy appears the most promising choice for the supervisory energy management of the vehicle. First of all, its analytical approach allows to make it enough flexible to cope with different objective

functions: the addition of ad-hoc penalty functions is straight-forward and only requiring the calibration of an additional weight factor. Of course, this is possible as long as the objective functions do not involve different state variables, which would instead make the algorithm more intricate.

The results show that it is possible to reduce the fuel consumption by 17.5% with an energy minimization-oriented strategy. In addition, ECMS is more effective to control both emissions and fuel economy. If a double target is applied, the fuel consumption is reduced to 5% while achieving Euro 6 emissions levels without the need for NOx and particulate matter aftertreatment systems. This strongly reduces the total cost of the propulsion system compared to a conventional vehicle, thus compensating the cost increase due to the hybridization without considering the fuel saving costs.

Acknowledgments

The authors acknowledge the Conselleria de Innovación, Universidades, Ciencia y Sociedad Digital de la Generalitat Valenciana for partially supporting this research through grant number GV/2020/017.

References

[1] Luján JM, García A, Monsalve-Serrano J, Martínez-Boggio S. Effectiveness of hybrid powertrains to reduce the fuel consumption and NOx emissions of a Euro 6d-temp diesel engine under real-life driving conditions. Energy Convers Manag 2019;199:111987. doi:10.1016/j.enconman.2019.111987.

[2] Serrano JR, García A, Monsalve-Serrano J, Martínez-Boggio S. High efficiency two stroke opposed piston engine for plug-in hybrid electric vehicle applications: Evaluation under homologation and real driving conditions. Appl Energy 2021;282:116078. doi:10.1016/j.apenergy.2020.116078.

[3] Borghi M, Mattarelli E, Muscoloni J, Rinaldini CA, Savioli T, Zardin B. Design and experimental development of a compact and efficient range extender engine. Appl Energy 2017;202:507–26. doi:10.1016/j.apenergy.2017.05.126.

[4] Altan A, Hacıoğlu R. Model predictive control of three-axis gimbal system mounted on UAV for real-time target tracking under external disturbances. Mech Syst Signal Process 2020;138. doi:10.1016/j.ymssp.2019.106548.

[5] Karasu S, Altan A, Bekiros S, Ahmad W. A new forecasting model with wrapper-based feature selection approach using multi-objective optimization technique for chaotic crude oil time series. Energy 2020;212:118750. doi:10.1016/j.energy.2020.118750.

[6] Li Z, Zhang Y, Huang G, Zhao W, He Z, Qian Y, et al. Control of intake boundary conditions for enabling clean combustion in variable engine conditions under intelligent charge compression ignition (ICCI) mode. Appl Energy 2020;274:115297. doi:10.1016/j.apenergy.2020.115297.

[7] Moradi J, Gharehghani A, Mirsalim M. Numerical investigation on the effect of

oxygen in combustion characteristics and to extend low load operating range of a natural-gas HCCI engine. Appl Energy 2020;276:115516. doi:10.1016/j.apenergy.2020.115516.

[8] Benajes J, García A, Monsalve-Serrano J, Balloul I, Pradel G. Evaluating the reactivity controlled compression ignition operating range limits in a high-compression ratio medium-duty diesel engine fueled with biodiesel and ethanol. Int J Engine Res 2017;18:66–80. doi:10.1177/1468087416678500.

[9] Singh AP, Kumar V, Agarwal AK. Evaluation of comparative engine combustion, performance and emission characteristics of low temperature combustion (PCCI and RCCI) modes. Appl Energy 2020;278:115644. doi:10.1016/j.apenergy.2020.115644.

[10] García A, Monsalve-Serrano J, Martinez-Boggio S, Gaillard P, Poussin O, Amer AA. Dual fuel combustion and hybrid electric powertrains as potential solution to achieve 2025 emissions targets in medium duty trucks sector. Energy Convers Manag 2020;224:113320. doi:10.1016/j.enconman.2020.113320.

[11] Abdul-Manan AFN, Won HW, Li Y, Sarathy SM, Xie X, Amer AA. Bridging the gap in a resource and climate-constrained world with advanced gasoline compression-ignition hybrids. Appl Energy 2020;267:114936. doi:10.1016/j.apenergy.2020.114936.

[12] Benajes J, García A, Monsalve-Serrano J, Martínez-Boggio S. Optimization of the parallel and mild hybrid vehicle platforms operating under conventional and advanced combustion modes. Energy Convers Manag 2019;190:73–90. doi:10.1016/j.enconman.2019.04.010.

[13] Molina S, García A, Monsalve-Serrano J, Villalta D. Effects of fuel injection parameters on premixed charge compression ignition combustion and emission characteristics in a medium-duty compression ignition diesel engine. Int J Engine Res 2021;22:443–55. doi:10.1177/1468087419867014.

[14] García A, Carlucci P, Monsalve-Serrano J, Valletta A, Martínez-Boggio S. Energy management strategies comparison for a parallel full hybrid electric vehicle using Reactivity Controlled Compression Ignition combustion. Appl Energy 2020;272:115191. doi:10.1016/j.apenergy.2020.115191.

[15] Bermúdez V, García A, Villalta D, Soto L. Assessment on the consequences of injection strategies on combustion process and particle size distributions in Euro VI medium-duty diesel engine. Int J Engine Res 2020;21:683–97. doi:10.1177/1468087419865652.

[16] Zhuang W, Li (Eben) S, Zhang X, Kum D, Song Z, Yin G, et al. A survey of powertrain configuration studies on hybrid electric vehicles. Appl Energy 2020;262:114553. doi:10.1016/j.apenergy.2020.114553.

[17] Rubino L, Capasso C, Veneri O. Review on plug-in electric vehicle charging architectures integrated with distributed energy sources for sustainable mobility. Appl Energy 2017;207:438–64. doi:10.1016/j.apenergy.2017.06.097.

[18] Sasaki S. Toyota's newly developed hybrid powertrain. IEEE Int Symp Power Semicond Devices ICs 1998:17–22. doi:10.1109/ispsd.1998.702540.

[19] Muta K, Yamazaki M, Tokieda J. Development of New-Generation Hybrid System THS II - Drastic Improvement of Power Performance and Fuel Economy 2019;2004.

[20] Yang Y, Hu X, Pei H, Peng Z. Comparison of power-split and parallel hybrid powertrain architectures with a single electric machine: Dynamic programming approach. Appl Energy 2016;168:683–90. doi:10.1016/j.apenergy.2016.02.023.

[21] Gan S, Chrenko D, Kéromnès A, Le Moyne L. Development of a Multi-Architecture and Multi-Application Hybrid Vehicle Design and Management Tool. Energies 2018;11:3185. doi:10.3390/en11113185.

[22] He H, Guo X. Multi-objective optimization research on the start condition for a parallel hybrid electric vehicle. Appl Energy 2018;227:294–303. doi:10.1016/j.apenergy.2017.07.082.

[23] Zou Y, Huang R, Wu X, Zhang B, Zhang Q, Wang N, et al. Modeling and energy management strategy research of a power-split hybrid electric vehicle. Adv Mech Eng 2020;12:168781402096262. doi:10.1177/1687814020962624.

[24] Benajes J, García A, Monsalve-Serrano J, Villalta D. Exploring the limits of the reactivity controlled compression ignition combustion concept in a light-duty diesel engine and the influence of the direct-injected fuel properties. Energy Convers Manag 2018;157:277–87. doi:10.1016/j.enconman.2017.12.028.

[25] Benajes J, Garcia A, Monsalve-Serrano J, Boronat V. Gaseous emissions and particle size distribution of dual-mode dual-fuel diesel-gasoline concept from low to full load. Appl Therm Eng 2017;120:138–49. doi:10.1016/j.applthermaleng.2017.04.005.

[26] Olmeda P, García A, Monsalve-Serrano J, Lago Sari R. Experimental investigation on RCCI heat transfer in a light-duty diesel engine with different fuels: Comparison versus conventional diesel combustion. Appl Therm Eng 2018;144:424–36. doi:10.1016/j.applthermaleng.2018.08.082.

[27] García A, Piqueras P, Monsalve-Serrano J, Lago Sari R. Sizing a conventional diesel oxidation catalyst to be used for RCCI combustion under real driving conditions. Appl Therm Eng 2018;140:62–72. doi:10.1016/j.applthermaleng.2018.05.043.

[28] Binder AJ, Toops TJ, Parks JE. Copper–Cobalt–Cerium Ternary Oxide as an Additive to a Conventional Platinum-Group-Metal Catalyst for Automotive Exhaust Catalysis. ChemCatChem 2018;10:1263–6. doi:10.1002/cctc.201701706.

[29] Binder AJ, Toops TJ, Unocic RR, Parks JE, Dai S. Low-Temperature CO Oxidation over a Ternary Oxide Catalyst with High Resistance to Hydrocarbon Inhibition. Angew Chemie - Int Ed 2015;54:13263–7. doi:10.1002/anie.201506093.

[30] Benajes J, García A, Monsalve-Serrano J, Boronat V. Achieving clean and efficient engine operation up to full load by combining optimized RCCI and dual-fuel

diesel-gasoline combustion strategies. Energy Convers Manag 2017;136:142–51. doi:10.1016/j.enconman.2017.01.010.

[31] Benajes J, Molina S, García A, Monsalve-Serrano J. Effects of direct injection timing and blending ratio on RCCI combustion with different low reactivity fuels. Energy Convers Manag 2015;99:193–209. doi:10.1016/j.enconman.2015.04.046.

[32] Benajes J, García A, Monsalve-Serrano J, Lago Sari R. Fuel consumption and engine-out emissions estimations of a light-duty engine running in dual-mode RCCI/CDC with different fuels and driving cycles. Energy 2018;157:19–30. doi:10.1016/j.energy.2018.05.144.

[33] Chung CT, Wu CH, Hung YH. Evaluation of driving performance and energy efficiency for a novel full hybrid system with dual-motor electric drive and integrated input- and output-split e-CVT. Energy 2020;191:116508. doi:10.1016/j.energy.2019.116508.

[34] Vinot E, Scordia J, Trigui R, Jeanneret B, Vinot E, Scordia J, et al. Model Simulation , validation and case study of the 2004 THS of Toyota Prius To cite this version : HAL Id : hal-02005586 2019.

[35] Liu J. Modeling, configuration and control optimization of power-split hybrid vehicles. The University of Michigan, 2007.

[36] Miller JM. Hybrid Electric Vehicle Propulsion System Architectures of the e-CVT Type. IEEE Trans Power Electron 2006;21:756–67. doi:10.1109/TPEL.2006.872372.

[37] Vinot E. Comparison of different power-split architectures using a global optimisation design method To cite this version : HAL Id : hal-01394060 2017.

[38] Muta K, Yamazaki M, Tokieda J. Development of new-generation hybrid system THS II - Drastic improvement of power performance and fuel economy. SAE Tech Pap 2004;2004. doi:10.4271/2004-01-0064.

[39] Liu J, Peng H. Modeling and Control of a Power-Split 2008;16:1242–51.

[40] Paganelli G. Conception et commande d'une chaîne de traction pour véhicule hybride parallèle thermique et électrique. Http://WwwThesesFr 1999.

[41] Venditti M. Analysis of the Performance of Different Machine Learning Techniques for the Definition of Rule-based Control Strategies in a Parallel HEV. Energy Procedia 2016;101:685–92. doi:10.1016/j.egypro.2016.11.087.

[42] Corbelli P. Hybrid e-CVT Power Split Drivelines. University of Bologna, 2011.

[43] Benford HL, Leising MB. The lever analogy: A new tool in transmission analysis. SAE Tech. Pap., SAE International; 1981. doi:10.4271/810102.

[44] Liao G. Using lever analogy diagrams in teaching compound planetary gear trains. ASEE Annu Conf Expo Conf Proc 2006.

[45] Liao YG, Chen M. Analysis of multi-speed transmission and electrically continuous variable transmission using lever analogy method for speed ratio

determination 2017;9:1–12. doi:10.1177/1687814017712948.

Abbreviations

ATS – After-Treatment System
BTE – Break Thermal Efficiency
CDC – Conventional Diesel Combustion
DI – Direct Injection
DOC – Diesel Oxidation Catalyst
DP – Dynamic Programming
ECMS – Equivalent Consumption Minimization Strategy
EGR – Exhaust Gas Recirculation
EM – Electric Machine
FHEV – Full Hybrid Electric Vehicle
GF – Gasoline Fraction
GM – General Motors
ICE – Internal Combustion Engine
LPS – Load Point Shifting
LTC – Low Temperature Combustion
MPRR – Maximum Pressure Rise Rate
NEDC – New European Driving Cycle
PFI – Port Fuel Injection
RCCI – Reactivity Controlled Compression Ignition
RDE – Real Driving Emission cycle
RBC – Rule-Based Control strategy
REESS – Rechargeable Electric Energy Storage System
SoC – State of Charge
THC – Total HydroCarbons
WLTC – World-wide harmonized Light-duty Test Cycle

Appendix A

In the configuration represented in Figure the ring gear and the planets internally mesh. The previous equations (1) – (10) apply for the HEV architecture represented in Figure A1, where the different gears of the planetary transmission are coupled to the power units: the sun gear to the EM1, the carrier to the ICE and the ring to the EM2.

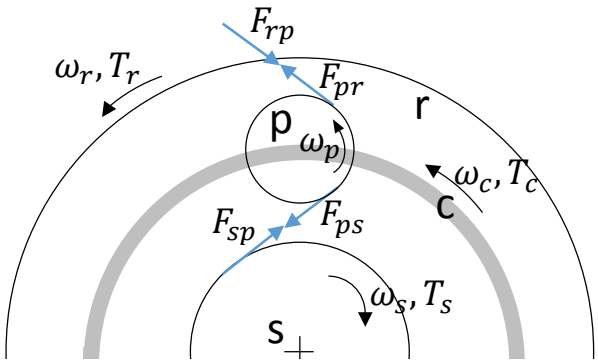

Figure A1 – Schematic diagram showing the transmission of forces in a planetary transmission. The letters s, p, c, r stand for sun, planet, carrier and ring respectively.

From considerations derived from the gears meshing relationships, the transmission ratio K between the ring gear and the sun gears can be used to characterize the planetary geartrain (a minus sign multiplies the transmission ratio since the primitive circumferences of the two gears are external to each other):

$$-K = K_{ring-planet} * -K_{planet-sun} = \frac{\omega_s}{\omega_r} = \frac{r_r}{r_s} = \frac{z_r}{z_s} = \frac{T_r}{T_s} \quad (A1)$$

Hence, using the Willis equation [41] provides the characteristic kinematic relation for the planetary transmission:

$$\omega_c = \frac{1}{(K+1)}\omega_s + \frac{K}{(K+1)}\omega_r \quad (A2)$$

Moreover, the dynamic equilibrium on the transmission is useful to derive the relationships between the exchanged torques:

$$T_s + T_c + T_r - T_{load} - J_s\dot{\omega}_s - J_c\dot{\omega}_c - J_r\dot{\omega}_r = 0 \quad (A3)$$

where T_{load} is the load torque applied at the transmission output, which corresponds to the shaft coupled to the ring gear of the transmission; J is the inertia of a gear. Also, the power balance can be written as follows:

$$(T_s - J_s\dot{\omega}_s)\omega_s + (T_c - J_c\dot{\omega}_c)\omega_c + (T_r - T_{load} - J_r\dot{\omega}_r)\omega_r = 0 \quad (A4)$$

Finally, combining the previous equations and making some simplifications results in a relationship between the torque applied on the sun gear and that one applied on the carrier gear:

$$T_s = J_s\dot{\omega}_s - \frac{1}{(K+1)}(T_c - J_c\dot{\omega}_c) \quad (A5)$$

Equation (5) can be interpreted as the torque which is transferred from the carrier to the sun or vice-versa, depending on the power flow: in this mechanical conversion there also are inefficiency losses which depend on the quality of the meshing between the sun and planets gears. To account for the meshing efficiency η_{ps}, equation (5) becomes:

$$T_s = J_s\dot{\omega}_s - \frac{1}{(K+1)}(T_c - J_c\dot{\omega}_c){\eta_{ps}}^q \quad (A6)$$

where the exponent $q = 1$ when the input torque is T_c, while $q = -1$ when T_s is the input torque. Substituting equation (6) into the torque equilibrium equation (3) it is also possible to obtain the relationship between the torque applied on the ring gear, the load torque and the one applied on the carrier:

$$T_r = T_{load} - \frac{K}{(K+1)}(T_c - J_c\dot{\omega}_c){\eta_{ps}}^q + J_r\dot{\omega}_r \quad (A7)$$

The second term of equation (7) stands for the torque that is transferred from the carrier to the ring. The efficiency of the meshing between planets and the ring gear η_{pr} may be considered, and the exponent $t = 1$ if the power flows from the transmission input to the ring output, and $t = -1$ when the power flow is opposite. Equation (7) can then be rewritten into equation (8):

$$T_r = T_{load} - \frac{K}{(K+1)}(T_c - J_c\dot{\omega}_c){\eta_{ps}}^q{\eta_{pr}}^t + J_r\dot{\omega}_r \quad (A8)$$

At steady state (i.e. no member is accelerating), the presented relations further simplify, as highlighted by the following system of equations:

$$\begin{cases} T_s = -\dfrac{1}{(K+1)} T_c {\eta_{ps}}^q \\ T_r = T_{load} - \dfrac{K}{(K+1)} T_c {\eta_{ps}}^q {\eta_{pr}}^t \end{cases} \quad (A9)$$

The system of equations (9) can be used to derive an equivalent set of relations in terms of power, since $T_s = P_s/\omega_s$, $T_c = P_c/\omega_c$, $T_r = P_r/\omega_r$, $T_{load} = P_{load}/\omega_r$:

$$\begin{cases} P_s = -\dfrac{1}{(K+1)} P_c \dfrac{\omega_s}{\omega_c} {\eta_{ps}}^q \\ P_r = P_{load} - \dfrac{K}{(K+1)} P_c \dfrac{\omega_r}{\omega_c} {\eta_{ps}}^q {\eta_{pr}}^t \end{cases} \quad (A10)$$

By using the kinematic relation of Willis (Equation 2), the system of Equation 10 can be used to understand the power flows in the transmission for different cases. In particular, it is noteworthy to observe what happens when one of the three members (i.e. sun, carrier, ring) is blocked, similarly to the study performed in [42]. It is possible to employ for this objective the lever analogy for planetary gear sets, which was introduced by Benford and Leising [43] and further exploited by Liao [44,45]: a gearset may be schematically replaced by a single vertical lever; the input, output, reaction torques are represented by horizontal forces that act on the lever and the angular velocities of the gears are represented by the lever motion relative to the reaction point. A rightward movement corresponds to clockwise rotation. The planetary transmission can be entirely represented with a vertical lever and its properties (i.e. the distance between the points of application of the forces) are determined by the characteristics of the gears in mesh, that are the number of teeth or the radii. The procedure to use the lever analogy for planetary gear sets was further exploited by Liao [44,45]. The relative rotational speeds can be calculated by treating the angular velocities as forces that act on the nodes of the lever, hence by applying the momentum equilibrium. The concept is better understood from Table 2.1, where it is put into practice for four representative operational cases, where for simplicity no load is applied on the output shaft (coupled to the ring gear) of the transmission.

Free members	Sun blocked	Carrier blocked	Ring blocked

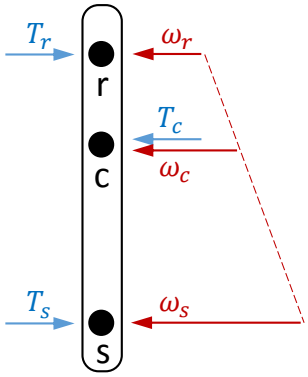	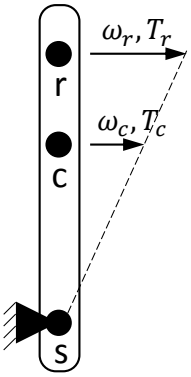	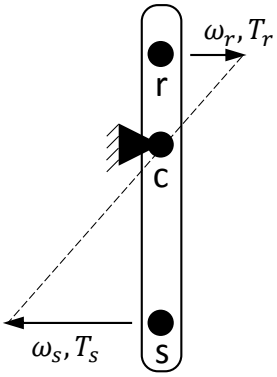	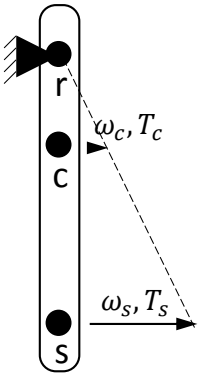
$-T_r(Z_s + Z_r) + T_c Z_r = 0$ $-T_r Z_s + T_s Z_r = 0$ $T_r - T_c + T_s = 0$ $T_r - T_c + T_s = 0$ $\frac{(\omega_r - \omega_s)}{(Z_s + Z_r)} = \frac{(\omega_c - \omega_s)}{Z_r}$	$T_r(Z_s + Z_r) + T_c Z_r = 0$ $\frac{\omega_r}{(Z_s + Z_r)} = -\frac{\omega_c}{Z_r}$	$T_r Z_s + T_s Z_r = 0$ $\frac{\omega_r}{Z_s} = -\frac{\omega_s}{Z_r}$	$T_s(Z_s + Z_r) + T_c Z_s = 0$ $\frac{\omega_s}{(Z_s + Z_r)} = -\frac{\omega_c}{Z_s}$

Table A1. Lever analogy applied on the planetary transmission for four representative operating conditions.